Introducing a Novel Optical Microcavity: A Glycerol/Water Microdroplet On a Superhydrophobic Surface

by

Mehmet Ali Dündar

A Thesis Submitted to the
Graduate School of Science
in Partial Fulfillment of the Requirements for
the Degree of

Master of Science
in
Physics

Koc University

July 2007

Koc University

Graduate School of Sciences and Engineering

This is to certify that I have examined this copy of a master's thesis by

Mehmet Ali Dündar

and have found that it is complete and satisfactory in all respects,
and that any and all revisions required by the final
examining committee have been made.

Committee Members:

_____

Alper Kiraz, Ph. D. (Advisor)

_____

Alphan Sennaroğlu, Ph. D.

_____

Adem Levent Demirel, Ph. D.

Date: _____

To my parents,
Ahmet and Nevin,

ABSTRACT

Optical microcavities confine light into small volumes in high quality resonances. They have found various applications in both fundamental and applied research areas such as cavity quantum electrodynamics, optoelectronics, and biological sensing. Up to date various geometries have been demonstrated to function as optical microcavities. Cylindrical, spherical, spheroidal/toroidal, ring, and other shapes and topologies with various confining principles have been used in these demonstrations.

With their specific truncated microsphere geometry, glycerol/water microdroplets standing on a superhydrophobic surface can also provide a three dimensional confinement for light, specifically in the equatorial plane paralel to the substrate. Provided a large contact angle, the whispering gallery modes (WGMs) of these optical microcavities can possess relatively high quality factors. Besides, no additional position control technique such as electrodynamic trapping or optical tweezing is necessary to analyze the optical properties of these microdroplets. In this thesis we present the following results obtained using single glycerol/water microdroplets standing on a superhydrophobic surface. (i) We demonstrate the observation of largely tunable WGMs in water microdroplets. Larger than 9.6 nm spectral tunability was achieved by evaporation/condensation in a current controlled mini humidity chamber. (ii) We demonstrate a self-control mechanism stabilizing the volume of these microdroplets with femtoliter resolution. The mechanism relied on the interplay between the condensation rate that was kept constant and the size dependent laser induced heating. By blocking the laser excitation for 500 msec, we were able to change the stable volume of individual microdroplets stepwise. (iii) We demonstrate lasing in Rhodamine B doped glycerol/water microdroplets. In these experiments, a pulsed, frequency-doubled Nd:YAG laser operating at 532 nm was used as the excitation source.

(iv) Using the same pulsed excitation source, we demonstrate Raman lasing in glycerol/water microdroplets.

The observed Raman lasing was not sustained; rather, oscillation would occur in temporally separated bursts. Inter-burst separations were determined to decrease from 2.3 sec to 0.4 sec by using nitrogen purging. Large spectral tunability of the WGMs can inspire novel applications in optical communication systems, e.g. tunable filters, switches, and lasers. The observed Raman lasing can also pave way to the development of very compact, cost-effective light sources for short-haul communications systems at around 650 nm. Besides due to the sensitivity of the WGMs to the size and shape of the microdroplets, our results can find applications in characterizing superhydrophobic surfaces and investigating liquid-solid surfaces.

ÖZET

Optik mikrokovuklar, ışığı küçük hacim içinde yüksek kaliteli rezonanslarda hapsederler. Bu yapılar, kovuk kuantum elektrodinamiği, optoelektronik ve biyolojik algılama gibi, temel ve uygulamalı araştırma alanlarında birçok uygulamalar bulmuşlardır. Bugüne kadar değişik şekillerin optik mikrokovuk işlevi gördükleri gösterilmiştir. Bu gösterimlerde çeşitli sınırlama ilkeleriyle silindirik, küresel, yuvarsı/toroid halka ve diğer şekiller ve topolojiler kullanılmıştır.

Kendilerine özgü kesik mikroküre şekilleriyle, su tutmayan yüzey üzerinde duran yağ/su mikrodamlacıkları da özellikle yüzeye paralel olan ekvatoral düzlemde ışık için üç boyutlu bir sınırlama sağlayabilirler. Büyük temas açılarıyla bu mikrokovukların fısıldayan galeri kipleri (FGKler) yüksek kalite faktörlerine sahip olabilirler. Bunun yanında, mikrodamlacıkların optik özelliklerini incelemek için elektrodinamik tutma ve optik cımbızlama gibi ek pozisyon kontrol tekniklerine ihtiyaç yoktur. Bu tezde, su tutmayan yüzey üzerinde duran basit gliserol/su mikrodamlacıkları kullanılarak elde edilen şu sonuçları sunuyoruz. (i) Su mikrodamlacıklarında geniş taranabilir FGKlerin gözlenmesi. 9.6 nm'den büyük tayf taranabilirliğine akımla kontrol edilen bir nem odacığı içinde buharlaşma/yoğunlaşma ile ulaşıldı. (ii) Su mikrodamlacıklarının kendi-kontrol mekanizmasıyla hacimlerini femtolitre seviyede sabit tutulabildiği gösterildi. Bu mekanizma, sabit tutulan yoğunlaşma oranı ile ebada bağlı lazer kaynaklı ısıtması arasındaki etkileşime dayanır. Uygulanan lazeri 500 milisaniye engelleyerek, sabit hacimli mikrodamlacıkların hacmini basamaklı olarak da değiştirebildik. (iii) Rhodamin B katılmış yağ/su mikrodamlacıkların lazer ışıması gösterildi. Bu deneyde, 532 nm'de çalışan iki kat sıklıklı darbeli bir lazer uyarma aracı olarak kullanıldı. (iv) Aynı uyarıcı kaynak kullanılarak yağ/su mikrodamlacıklarında Raman lazer ışıması gözlemlendi. Gözlenen Raman lazer ışıması, devamlı olmak yerine, aralıklı salınımlar şeklindeydi. Azot gazı

uygulanarak ışıma salınımlarının gözlenme aralıklarında 2.3 sn'den 0.4 sn'ye kadar düşme gözlemlendi.

FGKlerin yüksek tayf taranabilirliği; taranabilir filtreler, anahtarlar ve lazerler gibi optik iletişim sistemlerindeki yeni uygulamalara ilham verebilir. Gözlenen Raman ışıması 650 nm civarında kısa mesafeli iletişim sistemleri için çok düzenli, etkili fiyatta ışık kaynakları geliştirilmesine zemin hazırlayabilir. Bunun yanında sonuçlarımız FGKlerin damlacıkların büyüklüğüne ve şekline olan duyarlılığı sayesinde su tutmayan yüzeylerin karakterizasyonu ve sıvı-katı yüzeylerin incelenmesinde de uygulama bulabilir.

ACKNOWLEDGEMENTS

First and foremost, I would like to express my deepest gratitude to my academic advisor, assistant professor Alper Kiraz, for his continuous and valuable support and guidance he has provided me throughout my projects. He provided me invaluable help in planning and managing research projects. It was a great pleasure for me to conduct my projects under his supervision.

I would especially like to thank Mr. Adnan Kurt for his continuous support for my thesis.

I would like to thank Associate Prof. Adem Levent Demirel and Proffessor Alphan Sennaroglu for their support in my thesis. I am very grateful to be involved to conduct valuable experiments with them.

Special thanks also go to Mehdi Yavuz Yüce for simulating our experiments in Matlab and Mathematica. I am also thankful to him for his support before my thesis defence.

I would like to gratefully acknowledge Sultan Doğanay, Micheal Boyman, Alican Mert, Serhat Yavuz Okumuş, Ismail Enes Uysal and research students of Science 150 (Laser Research Laboratory) for their contributions and help during my thesis work.

I would like to thank Esra Özel, Mustafa Yıldırım, Gürhan Çapar, Ahmet Akın Ünal, K. Onur Unutulmaz, Naci Yıldız, Bora Akçay, Nihat Bilgin, Mehmet Akgül for their endless encouragements and motivations.

LIST OF FIGURES

NOMENCLATURE

WGM	whispering gallery mode
TE	transverse electric
TM	transverse magnetic
n	mode number
l	mode order
Q	quality factor
FSR	free spectral range
FWHM	full width at half maximum
λ	wavelength
Q_{abs}	absorption efficiency
$\widetilde{Q}_{abs}$	modified absorption efficiency
NA	numerical aperture
LE 1	lotus effect 1
LE 2	lotus effect2
CERS	cavity enhanced Raman scattering

Chapter 1

INTRODUCTION

1.1. Overview

Optical microcavities confine light into small volumes in high quality resonances. Up to date various geometries have been demonstrated to function as optical microcavities. Cylindrical, spherical, spheroidal/toroidal, ring, and other shapes and topologies with various confining principles have been used in these demonstrations [1]. Examples include fabry-perot resonators [2], microdisks [3], microrings [4], microspheres [5], annular Bragg microcavities [6], microtoroids [7], micropillars [8], photonic crystal defect microcavities [9], and microdroplets [10]. Optical microcavities have so far found various applications in both fundamental and applied research areas such as cavity quantum electrodynamics, optoelectronics, and biological sensing [11].

Applications in cavity quantum electrodynamics are based on the large coupling constants of the optical microcavity resonances to a resonant dipole emitter. Notable demonstrations have been performed in quantum optics, among which are very low threshold lasers [12], Purcell effect and vacuum Rabi splitting [11].

In optoelectronics optical microcavities are attractive for numerous applications. High quality resonances make optical microcavities extremely wavelength selective. They are therefore ideally suited for applications as optical filtering/switching in wavelength division multiplexed optical communications networks.

In biology, optical microcavities promise to function as highly sensitive biological sensors. They have attracted much attention for detecting biological molecules due to: 1) high sensitivity 2) non-destructiveness to the sample; 3) high selectivity; and 4) applicability to various substances [1]. Those applications have been achieved by detecting spectral changes in optical microcavity resonances caused by biological molecules attached to the microcavity's surface. Due to the high quality resonances, minute spectral changes corresponding to very small amounts of biological molecules can be detected.

The tendency of liquid droplets to minimize interfacial energy by minimizing the interfacial area results in nearly spherical shapes in air. This inspired their use as microsphere microcavities. In their pioneering work, Ashkin and Dziedzic used suspending single liquid microdroplets in air by optical levitation [13]. They observed whispering gallery modes (WGMs) by analyzing the laser power required to stabilize the height of the microdroplets as a function of wavelength [14]. Liquid droplet characterization for diagnostic purposes was also developed for a wide range of sizes, and selected imaging of various liquid phase constituents of a spray using two-dimensional fluorescence, lasing, and stimulated Raman scattering was reported. Electrodynamic levitation and optical tweezing were also used in position stabilization of microdroplets [15].

In this thesis we introduce a glycerol/water microdroplet standing on a superhydrophobic surface (Figure 1.1) as a novel optical microcavity. Due to the superhydrophobic nature of the surface, the spherical structure of the droplets is well maintained and a mode structure similar to that of an ideal spherical resonator can be obtained [16]. The technique used allows for the analysis of a particular microdroplet over prolonged periods without the need of a complex position stabilization mechanism such as electrodynamic levitation and optical tweezing. As demonstrated in the following chapters these microdroplets can be attractive alternatives to solid optical microcavities standing on substrates, e.g. microdisks, micropillars, and photonic crystal defect microcavities.

Microdroplets standing on a superhydrophobic surface do not pose any microfabrication challenges. They also bring together the advantage of easy deformability.

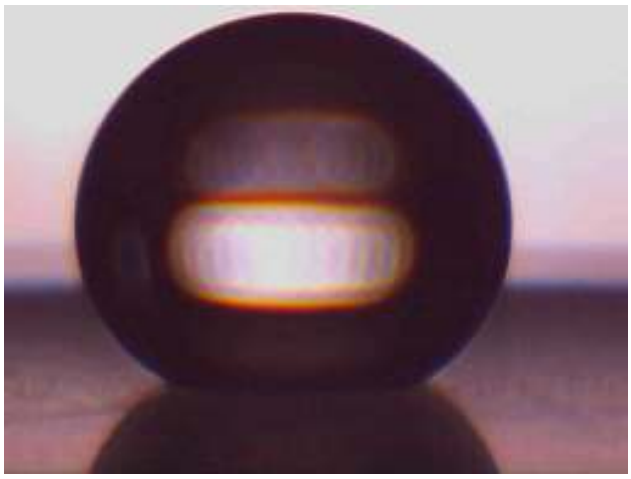

Figure 1. 1 A millimeter size water microdroplet standing on a superhydrophobic surface

1.2. Thesis Outline

Superhydrophobic surface preparation and experimental setup are presented in C**hapter 1**.

Chapter 2 contains the computational treatment of the resonances of an ideal dielectric microsphere. The analytical solutions of the Mie and Generalized Lorenz Mie theory are demonstrated for the case of plane wave and arbitrary wave illumination.

Chapter 3 demonstrates the observation and tunability of whispering gallery modes of a water microdroplet standing on a superhydrophobic surface. Tunability was achieved by changing humidity level inside the humidity chamber resulting condensation and evaporation of the microdroplets.

Chapter 4 demonstrates a self control mechanism that stabilizes the volume of individual water microdroplets with femtoliter resolution. The reported volume stabilization mechanism relied on the interplay between the ambient humidity and the laser induced heating. Volume stabilization conditions are also characterized and simulated by computational results.

Chapter 5 describes low threshold lasing in single glycerol/water microdroplets doped by Rhodamine B dye molecules. In these experiments optical pumping was done with a Q-switched laser source.

Chapter 6 shows the Raman lasing from glycerol/water microdroplets. In these experiments two distinct operation regimes were observed: cavity-enhanced Raman scattering and Raman lasing near 630 nm. In the latter case, Raman lasing signal was higher than the background by more than 30 dB. Raman lasing was not sustained; rather, oscillation would occur in temporally separated bursts.

1.3 Surface Preparation and Contact Angle Measurements

Superhydrophobic surfaces were prepared by spin coating a 20-60 mg/ml ethanol dispersion of hydrophobically coated silica nanoparticles on cover glasses at 2000 rpm for 1 minute [17]. Hydrophobically coated silica nanoparticles (Degussa AG Aeroxide LE1 or LE2) had an average particle size diameter of 20 nm and 7 nm respevtively. Resulting superhydrophobic surfaces had nanometer scale surface roughness and were transparent to visible light. The average contact angle of millimetric water droplets on the superhydrophobic surface was measured to be >150°. Prepared substrates were post-baked in an oven at 70 °C for one hour, for evaporation of the remaining ethanol.

The angle between the liquid-vapor or liquid-solid interfaces is called contact angle and denoted by θ. Three regimes can be analyzed by the contact angle measurement, partial wetting ($\theta \leq 90^0$), non-wetting ($\theta \geq 90$) and transition regime ($\theta = 90^0$). Surfaces with a contact angle $\theta \geq 150$ are called superhydrophobic. The contact angle can be measured by using Young's or Cassie equation [17].

For commercially available two different silica nanoparticles (Degussa AG Aeroxide LE1 and LE2) surface roughness appear different. Surface roughness can be analyzed by using BET (Brunauer, Emmett and Teller) surface area and tamped density[18]. BET is defined as the surface area of precipitated silica and the tamped density defined as the initial weight of the sample and the resulting volume. The BET surface area and the tamped density of LE1 is found as 160 m^2/g and 140 g/l whereas LE 2 has 190-250 m^2/g BET surface area and 60 g/l tamped density. The difference on the damped density has significant effect on the contact angle change due to surface roughness (Section 3.1.4).

1.4 Experimental Setup and Microdroplet Generation

A continuous wave (Chapters 3 and 4) or pulsed (Chapters 5 and 6, pulsewidth=100 ns, repetition rate=1 kHz) solid state green laser (λ=532 nm) was used to excite the microdroplets. The continuous wave laser was focused to a resolution limited spot near the outer surface while the pulsed laser was focused to a diameter of 14 μm (Chapter 5) or 28 μm (Chapter 6). Excitation of the microdroplets and the collection of the emission were done by a high numerical aperture microscope objective (NA=1.4, 60x for Chapters 3 and 4; NA=0.88 for Chapters 5 and 6). After being transmitted through a dichroic mirror

(Q570LP), and a 1.5x magnifier element, the collected fluorescence was dispersed using a 50 cm monochromator and detected by a charged coupled device camera, as in figure 1.2.

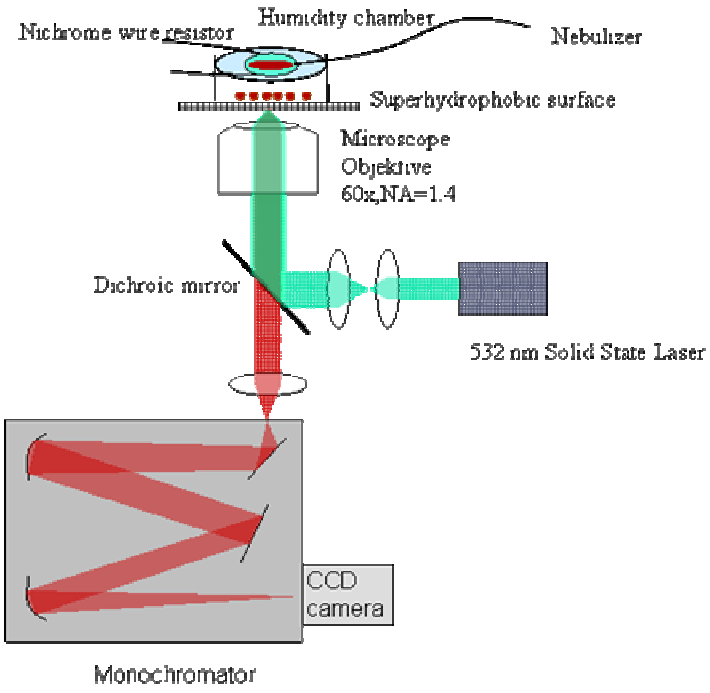

Figure 1. 2 Experimental Setup

Microdroplets are generated by an ultrasonic nebulizer (Chapters 3 and 4) and an atomizer (Chapters 5 and 6). The droplets are doped by different concentrations of Rhodamine B dye molecules. The measured absorption and emission spectra of Rhodamine B are shown in Fig.s 1.3 and 1.4 respectively. For Chapters 3 and 4 Rhodamine B doped water droplets are kept in a home-built current controlled mini humidity chamber. In contrast, a humidity chamber was not used in the experiments perfomed on glycerol/water microdroplets (Chapters 5 and 6). These microdropelts were kept in contact with the

ambient atmosphere after their generation. Once sprayed, they quickly evaporated, and reached their equilibrium sizes.

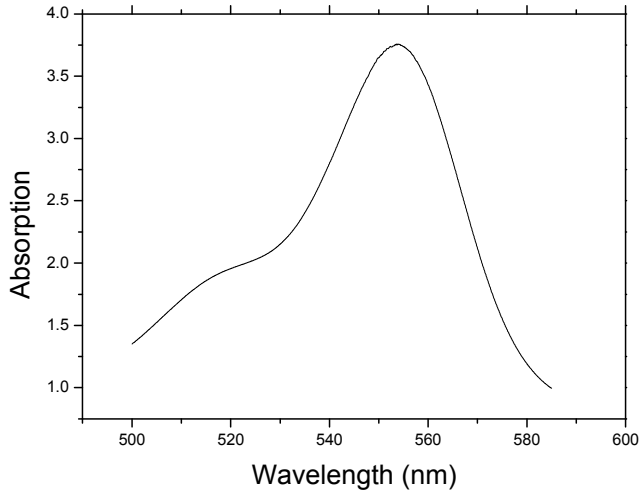

Figure 1. 3 Absorption spectra of 25 μM Rhodamine B dye molecules

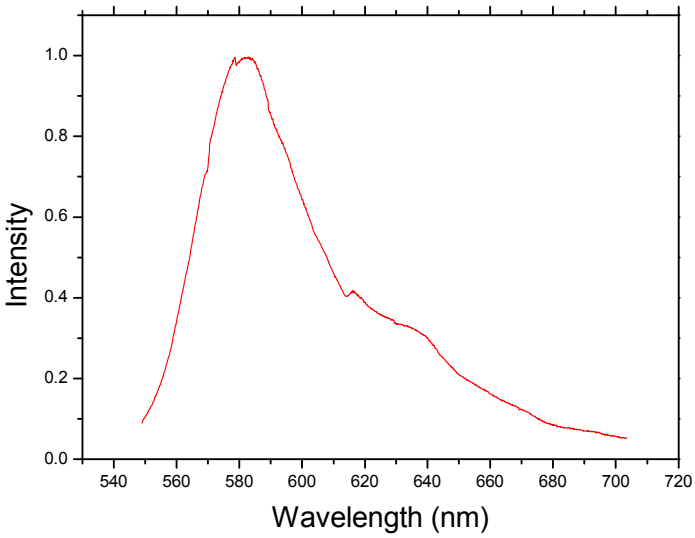

Figure 1. 4 Emission spectra of 25 μM Rhodamine B dye molecules

Chapter 2

CALCULATION OF OPTICAL MODES OF A DIELECTRIC SPHERE

2.1 Introduction

The history of investigation of optical modes of a dielectric sphere was started by Mie at the beginning of 19^{th} century. He investigated the absorption and scattering of plane electromagnetic waves incident upon a dielectric sphere of arbitrary radius and refractive index. The calculated spectrum of the electromagnetic wave showed sharp features which could be attributed to resonant circulation of optical energy. These resonances are called as whispering gallery modes. In this chapter we derive the analytic formulas revealing the WGMs of a dielectric microsphere.

Mie theory can be extended to study the absorption of arbitrary electromagnetic beams by dielectric microspheres. Such a calculation reveals the sensitivity of the absorption spectrum to the position of the focal point. In this chapter we also summarize the formulation used by Barton[19],[20]. We present the calculations performed considering spherical microdroplets. As it will be discussed in Chapter 4, the resonances observed in laser absorption play crucial roles in the realization of the volume stabilization schema.

2.2 The Mie theory for Plane Wave Calculation

Maxwell equations for a time harmonic electromagnetic field in a linear, isotropic, homogeneous medium is described as,

$$\nabla.\vec{E} = 0\,,\ \nabla.\vec{H} = 0\,,\ \nabla\times\vec{E} = i\omega\mu\vec{H} \text{ and } \nabla\times\vec{H} = -i\omega\mu\varepsilon\vec{E} \tag{2.1}$$

In the above equation μ is the permeability and ε is the permittivity of the medium. The term ω comes from time varying factor of the wave, $\exp(-i\omega t)$. This factor will be suppressed in the later derivations and formulas. The electromagnetic wave has two components, electric field and magnetic field, satisfying Helmothz equation as;

$$\nabla^2\vec{E} + k^2\vec{E} = 0 \text{ and } \nabla^2\vec{H} + k^2\vec{H} = 0 \tag{2.2}$$

Where $k = \omega\sqrt{\mu\varepsilon}$

Since the sphere is homogenously dielectric and the optical modes reflect with grazing incidence upon the dielectric-air boundary, the modes can be solved as the result of scalar wave approximation, as transverse electric (TE) and transverse magnetic (TM), which posses an electric or a magnetic field parallel to the surface of the sphere respectively[1][21]. When we plug the Helmothz equation (2.2) in spherical polar coordinates using the scalar wave approximation, we obtain;

$$\frac{1}{r^2}\frac{\partial}{\partial r}\left(r^2\frac{\partial\eta}{\partial r}\right) + \frac{1}{r^2\sin\theta}\frac{\partial}{\partial\theta}\left(\sin\theta\frac{\partial\eta}{\partial\theta}\right) + \frac{1}{r^2\sin\theta}\frac{\partial^2\eta}{\partial\phi} + k^2\eta = 0 \tag{2.3}$$

[1] i.e $E_\phi = E_r = 0$ and $H_\phi = H_r = 0$

The wave has particular solution defining as $\eta(r,\theta,\phi) = \eta_r(r)\eta_\theta(\theta)\eta_\phi(\phi)$, where the solutions are described in radial, polar and the azimuthal components. When we plug the above equation into (2.3), one can obtain;

The radial component,

$$\frac{d}{dr}(r^2 \frac{d\eta_r}{dr}) + \left[k^2 r^2 - n(n+1)\right]\eta_r = 0 \tag{2.4}$$

The polar component,

$$\frac{1}{\sin\theta}\frac{d}{d\theta}(\sin\theta \frac{d\eta_\theta}{d\theta}) + \left[n(n+1) - \frac{m^2}{\sin^2\theta}\right]\eta_\theta = 0 \tag{2.5}$$

The azimuthal component,

$$\frac{d^2\eta_\phi}{d\phi} + m^2\eta_\phi = 0 \tag{2.6}$$

The linearly independent solution of (2.4) is obtained by any two linear combinations of the spherical Bessel function of first and second kind where introducing a dimensionless variable $\rho = kr$. The linear combination is called spherical Hankel function or spherical Bessel function of the third kind[2].

The linearly independent solution of (2.5) can be achieved by introducing the associated legendre functions of the first kind $P_n^m(\cos\theta)$ of degree n and order m, where $n = m, m+1, m+2...$

$$P_n^m(\cos\theta) = (-1)^m(1-\cos^2\theta)^{m/2}\frac{d^m}{d(\cos\theta)^m}P_n(\cos\theta) \tag{2.7}$$

[2] Spherical Bessel of first, second and spherical Hankel funciton of first and second kind are respectively as:
$J_n^{(1)}(\rho) = (\sqrt{\pi/2\rho})J^{(1)}{}_{n+0.5}(\rho)$, $J_n^{(2)}(\rho) = (\sqrt{\pi/2\rho})J^{(2)}{}_{n+0.5}(\rho)$,
$H_n^{(1)}(\rho) = J^{(1)}(\rho) + iJ^{(2)}(\rho)$ and $H_n^{(2)}(\rho) = J^{(1)}(\rho) - iJ^{(2)}(\rho)$

and $$P_n(\cos\theta) = \frac{1}{2^n n!}\frac{d^n}{d(\cos\theta)^n}\left[\cos^2\theta - 1\right]^n \tag{2.8}$$

The solution of (2.5) is even and odd functions as[3];

$$\eta_\phi{}^e = \cos m\phi \text{ and } \eta_\phi{}^o = \sin m\phi \tag{2.9}$$

Inserting the solutions (2.5), (2.7) and (2.9) into scalar wave equation we get[4]

$$\eta_{mn}^e = \Lambda_n(\rho)P_m^n(\cos\theta)\cos m\phi \tag{2.10a}$$

$$\eta_{mn}^o = \Lambda_n(\rho)P_m^n(\cos\theta)\sin m\phi \tag{2.10b}$$

2.2.1 The Plane Wave Calculation

After calculating the scalar wave equation, to find the field inside the dielectric sphere and scattered field, we assume that incident wave is propagating in $+z$ direction and $x-$polarized.

When we impose the boundary condition between the sphere and the air, the tangential component of the electric and magnetic wave can be written in the form as;

$$(E_i + E_s - E_{inside}) \times \hat{r} = 0 \text{ and } (H_i + H_s - H_{inside}) \times \hat{r} = 0 \tag{2.11}$$

For a given scalar wave function, one can convert it into vector spherical harmonics[5]. Since vector harmonics will consist of associated Legendre polynomials, the

[3] Here superscript e and o describes even and odd functions respectively.

[4] Here Λ is any linearly independent equation of four spherical functions in described in footnote 2

orthogonality condition is achieved. Another orthogonality is achieved by setting $m \neq 1$. Moreover, because of the completeness of the functions in (2.10a) and (2.10b), the spherical polar coordinates can be expanded as an infinite series. This leads us to write all electric and magnetic fields, inside the sphere, scattered and incident can be expanded as infinite series with some coefficients. These coefficients include both incoming wave, described by spherical Bessel functions and spherical Hankel functions because it describes spherical waves propagating outside the spherical object. Using the boundary conditions on both polar and azimuthal components of electric and magnetic wave, these coefficients are written as a_n, b_n as scattered coefficients, c_n, d_n as internal field coefficients[19].

$$a_n = \frac{\mu m^2 j_n^{(1)}(x)\left[x j_n^{(1)}(x)\right]' - \mu_1 j_n^{(1)}\left[mx j_n^{1}(mx)\right]'}{\mu m^2 j_n^{(1)}(mx)\left[x h_n^{(1)}(x)\right]' - \mu_1 h_n^{(1)}(x)\left[mx j_n^{(1)}(mx)\right]'} \tag{2.12a}$$

$$b_n = \frac{\mu_1 j_n^{(1)}(mx)\left[x j_n^{(1)}(x)\right]' - \mu j_n^{(1)}\left[mx j_n^{1}(mx)\right]'}{\mu_1 j_n^{(1)}(mx)\left[x h_n^{(1)}(x)\right]' - \mu h_n^{(1)}(x)\left[mx j_n^{(1)}(mx)\right]'} \tag{2.12b}$$

By using these equations, the scattered electric field and the scattered magnetic field in spherical harmonics and infinite series can be written as;

$$E_s = \sum_n^{\infty} i^n E_0 \frac{2n+1}{n(n+1)} (i a_n G_{1n}^{e(3)} - b_n F_{1n}^{o(3)}) \tag{2.13a}$$

$$H_s = \frac{k}{\omega\mu} \sum_n^{\infty} i^n E_0 \frac{2n+1}{n(n+1)} (i b_n F_{1n}^{o(3)} - a_n G_{1n}^{e(3)}) \tag{2.13b}$$

[5] The conversion of spherical harmonics can be obtained to take the curl of the scalar wavefunciton which is multiplied by the position vector.

The coefficients of the field inside the sphere can be determined by using the same boundary condition. Then the coefficients become,

$$c_n = \frac{\mu_1 j_n^{(1)}(x)\left[xh_n^{(1)}(x)\right]' - \mu_1 h_n^{(1)}\left[xj_n^{1}(x)\right]'}{\mu_1 j_n^{(1)}(mx)\left[xh_n^{(1)}(x)\right]' - \mu h_n^{(1)}(x)\left[mxj_n^{(1)}(mx)\right]'} \tag{2.14a}$$

$$d_n = \frac{\mu_1 m j_n^{(1)}(x)\left[xh_n^{(1)}(x)\right]' - \mu_1 m h_n^{(1)}\left[xj_n^{1}(x)\right]'}{\mu m^2 j_n^{(1)}(mx)\left[xh_n^{(1)}(x)\right]' - \mu_1 h_n^{(1)}(x)\left[mxj_n^{(1)}(mx)\right]'} \tag{2.14b}$$

Then the internal field is represented as,

$$E_{inside} = \sum_n^{\infty} i^n E_0 \frac{2n+1}{n(n+1)}(c_n F_{1n}^{o(1)} - id_n G_{1n}^{e(1)}) \tag{2.15a}$$

$$H_{inside} = \frac{-k_1}{\omega\mu_1}\sum_n^{\infty} i^n E_0 \frac{2n+1}{n(n+1)}(d_n F_{1n}^{e(1)} + ic_n G_{1n}^{e(1)}) \tag{2.15b}$$

In the above equations the superscript (1) and (3) denote the vector spherical harmonics specified by $J_n^{(1)}(kx)$ where k represents the wave-vector of the scattered field and the vector spherical harmonics specified by $h_n^1(k_{inside}x)$ where k_{inside} is the wave vector of the field inside the sphere. The primes denote the differentiation with respect to the argument in the parentheses. Here x is the size parameter defined as $x = ka$ and the m is the relative refractive index, the ratio of the inside wave-vector to the scattered wave-vector. μ_1 and μ are the permeability of the sphere and the surrounding medium respectively.

From the equation (2.13a) and (2.13b), one can say that the conditions of the resonance modes of nth mode electric and magnetic wave can be achieved by setting the denominator to zero. These modes (TM and TE) are characterized by whether a_n or b_n are dominant to each other respectively.

If a_n is dominant which corresponds to TM case;

$$\frac{\left[xh_n^{(1)}(x)\right]'}{h_n^{(1)}(x)} = \frac{\mu_1\left[mxj_n^{(1)}(mx)\right]'}{\mu m^2 j_n^{(1)}(mx)} \tag{2.16a}$$

If b_n is dominant which corresponds to TE case

$$\frac{\left[xh_n^{(1)}(x)\right]'}{h_n^{(1)}(x)} = \frac{\mu\left[mxj_n^{(1)}(mx)\right]'}{\mu_1 j_n^{(1)}(mx)} \tag{2.16b}$$

2.3 Whispering Gallery Modes

Whispering gallery modes, sometimes called morphology dependent resonances, are named after the whispering gallery at St. Paul's cathedral in London after Lord Rayleigh's work [22] on sound propagation over a curved gallery surface. A little bit earlier, Debye demonstrated the equations of resonant eigenfrequencies of free dielectric and metallic spheres. Those equations can be deducted by Mie, as in the previous chapter.

Whispering gallery modes occur at particular resonant wavelengths of light which is confined to spherical volume with a greater refractive index than the surrounding medium has. Due to high refractive index contrast, the light undergoes by total internal reflection. By achieving minimal reflection losses, WGMs at those wavelengths can have high quality factors.

The WGMs have two linearly independent solutions of Helmothz equation as transverse electric (TE) and transverse magnetic (TM). These modes are characterized by a polar mode number, n, and a radial mode order l for a dielectric sphere figure 2.1 and

figure 2.2. The mode number shows us the number of wavelengths occurring around the circumference of the particle whereas mode order shows the number of maxima in the radial dependence of the electromagnetic field within the volume.

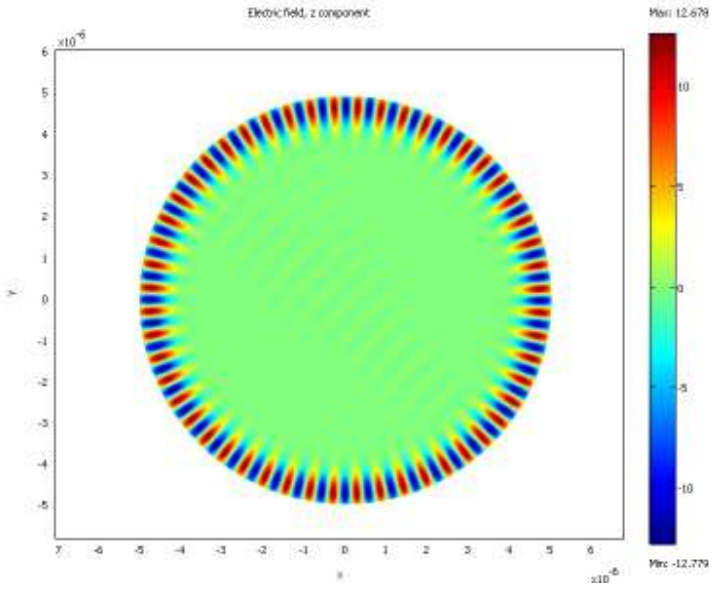

Figure 2. 1 Femlab simulation of a microdisk with a radius 5 μ m having $TE_{26,1}$

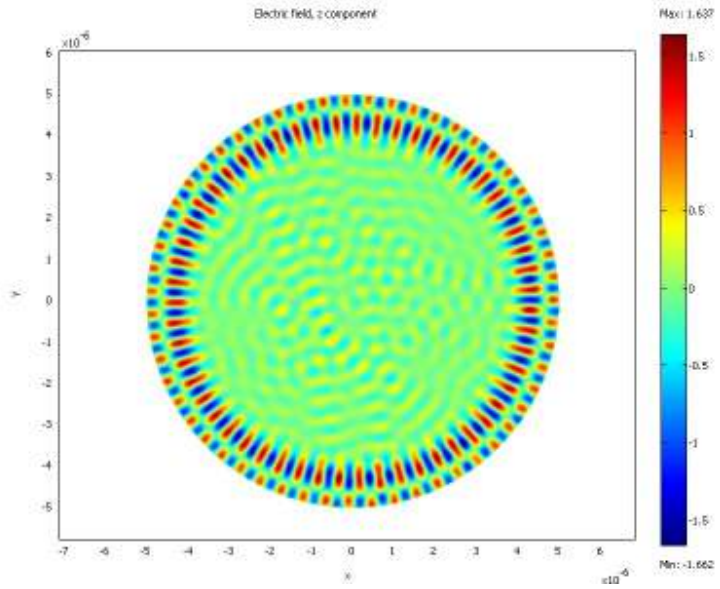

Figure 2. 2 Femlab simulation of a microdisk with a radius 5 μ m having $TE_{27,2}$

The first observation of WGMs were done by investigating elastic light scattering from spherical dielectric particles in liquid resonators[23, 24],[13]. After this observation, it was recognized that WGMs could help in measurements of spherical particle size, shape, refractive index and temperature [25], [14]. Then WGMs have attracted much attention due to the potential applications in the field of atom optics, photonics, cavity quantum electrodynamics and modern telecommunications. Some applications are realization of microlasers, narrow filters[26], tunable filters [27], optical switching [28], high resolution spectroscopy, investigating Purcell factor, Raman sources and studies on nonlinear optics [16], [29].

2.4 Characterizations of Whispering Gallery Modes

The basic parameters defining the characteristics of a resonator are quality (Q) factor, mode volume, and mode spacing between resonances.

2.4.1 Quality Factor

The quality factor is the basic parameter to characterize the mode. The quality (Q) factor determines how long a photon can be stored inside a resonator. This is also related to the lifetime of light energy in the resonator mode (τ) and described as $Q = \omega\tau$, where ω is the frequency of the mode. Alternatively, sharpness of the mode is also described by the Q-factor. In this case, the ratio of the wavelength hosting the mode over the linewidth gives Q-factor, as $Q = \lambda / \Delta\lambda_{1/2}$, where λ is the wavelength and $\Delta\lambda_{1/2}$ is the linewidth. So far maximum $Q = 2 \times 10^{10}$ has been achieved by using crystalline resonator[30].

2.4.2 Mode Volume

Another basic parameter of a WGM is the mode volume (field localization). The most common definition of mode volume is related to energy density of the optical mode. Mode volume can be defined as;

$$V_{\mathrm{mod}e} = \frac{\int \varepsilon \left|\vec{E}\right|^2 dV}{\max \varepsilon \left|\vec{E}\right|^2} \tag{2.17}$$

There are different characteristics about mode volume for different kind of resonators. Resonators with the smallest mode volumes have been realized in photonic crystal resonators[9], microdisk [31], [32].

2.4.3 Mode Spacing

Mode spacing defined as the wavelength difference between two identical polarized consecutive mode numbers n and in the same mode order l obtained as;

$$\lambda_{n+1,l} - \lambda_{n,l} = \frac{\lambda^2}{2\pi a} \frac{\tan^{-1}(\sqrt{m^2 - 1})}{\sqrt{m^2 - 1}} \tag{2.18}$$

The second term on the right hand side is the inverse of the effective refractive index as in Fabry-Perot resonators.

2.5 Absorption Cross Section and Absorption Efficiency of a Dielectric Sphere

The absorption cross section of a particle with dielectric losses, i.e. Ohmic, is given as [33];

$$\sigma_{abs} = k\varepsilon'' \pi \int_V \left| E_{inside} \right|^2 dV \tag{2.19}$$

where ε'' is the imaginary part of the relative dielectric constant of the particle with respect to the medium. For over all volume up to radius a, the integrand results absorption efficiency. The absorption efficiency is defined as the absorbed total power by the particle over the power incident on the projected area of the sphere [19]. The efficiency is expressed by the incident plane wave coefficients as;

$$Q_{abs} = \frac{2}{\alpha^2}\sum_{n=1}^{\infty}(2n+1)\left[\mathrm{Re}(a_n + b_n) - (|a_n|^2 + |b_n|^2)\right] \tag{2.20}$$

2.6 The Generalized Lorenz Mie Theory for Arbitrary Beam Calculation.

In section 2.2, we demonstrated the internal and scattered field of a spherical object in which there is a plane wave electromagnetic beam incident upon it. In this part the generalized Lorenz Mie theory for an arbitrary electromagnetic beam approach is demonstrated. We consider the beam as linear, isotropic, nonmagnetic, non-electrically conducting incident upon an isotropic, linear homogenous sphere with radius a. The calculations of internal and scattered field coefficients of this type electromagnetic beam are the same as in section 2.2. the electric and magnetic field components are given as

$$\begin{aligned} E_r &= \frac{\partial^2(r^e\Pi)}{\partial r^2} + k^2 r^e\Pi, E_\theta = \frac{1}{r}\frac{\partial^2(r^e\Pi)}{\partial\theta\partial r} + \frac{k''}{r\sin\theta}\frac{\partial(r^m\Pi)}{\partial\phi}, \\ E_\phi &= \frac{1}{r\sin\theta}\frac{\partial^2(r^e\Pi)}{\partial\phi\partial r} - \frac{k''}{r}\frac{\partial(r^m\Pi)}{\partial\theta} \end{aligned} \tag{2.21}$$

$$\begin{aligned} H_r &= \frac{\partial^2(r^m\Pi)}{\partial r^2} + k^2 r^m\Pi, H_\theta = \frac{-k'}{r}\frac{\partial^2(r^e\Pi)}{\partial\theta} + \frac{1}{r}\frac{\partial(r^m\Pi)}{\partial r\partial\theta}, \\ H_\phi &= \frac{k'}{r}\frac{\partial^2(r^e\Pi)}{\partial\theta} + \frac{1}{r\sin\theta}\frac{\partial(r^m\Pi)}{\partial r\partial\phi} \end{aligned} \tag{2.22}$$

where $k' = ik_0\tilde{\varepsilon}, k'' = ik_0$ and $k = k_0\sqrt{\tilde{\varepsilon}}, k_0 = \frac{w}{c}$. Both ${}^e\Pi$ and ${}^m\Pi$ satisfies Helmothz equation.

After this part the calculation for the solution of an arbitrary beam differs from the plane wave solution. The wave equation which obeys Helmoths equation is,

$$r\Pi = \sum_{l=0}^{\infty}\sum_{m=-l}^{l}\left[\widetilde{A}_{lm}\psi_l(kr) + \widetilde{B}_{lm}\chi(kr)\right]Y_{lm}(\theta,\phi) \tag{2.23}$$

where $\widetilde{A}_{lm}$ and $\widetilde{B}_{lm}$ are arbitrary complex constant, ψ and χ are Ricatti-Bessel functions and Y_{lm} is the spherical harmonic function. The indices l and m are integers and represent radial and angular mode. The coefficients of scattered and internal field of electric and magnetic wave l th radial mode and m th angular mode differ from (2.12) and (2.13) by the factor A_{lm} and B_{lm} .The new coefficients are described as $a_{lm} = -a_l A_{lm}$ and $b_{lm} = -b_l B_{lm}$. A_{lm} and B_{lm} are incident field coefficients which are characteristic for the incident beam and are defined as;

$$A_{lm} = \frac{a^2}{l(l+1)\psi_l(k_{ext}a)}\int_0^{2\pi}\int_0^{\pi}\sin\theta E_r^{(incident)}(a,\theta,\phi)\times Y_{lm}^{*}(\theta,\phi)d\theta d\phi \tag{2.24.a}$$

$$B_{lm} = \frac{a^2}{l(l+1)\psi_l(k_{ext}a)}\int_0^{2\pi}\int_0^{\pi}\sin\theta H_r^{(incident)}(a,\theta,\phi)\times Y_{lm}^{*}(\theta,\phi)d\theta d\phi \tag{2.24.b}$$

The coefficients for scattered fields and internal fields become respectively

$$a_{lm} = \frac{\psi_l'(k_{\text{int}}a)\psi(k_{ext}a) - \overline{n}\,\psi_l(k_{\text{int}}a)\psi_l'(k_{ext}a)}{\overline{n}\,\psi_l(k_{\text{int}}a)\xi_l^{(1)}(k_{ext}a) - \psi_l'(k_{\text{int}}a)\xi_l^{(1)}(k_{ext}a)}A_{lm} \tag{2.25.a}$$

$$b_{lm} = \frac{\overline{n}\,\psi_l'(k_{\text{int}}a)\psi(k_{ext}a) - \psi_l(k_{\text{int}}a)\psi_l'(k_{ext}a)}{\psi_l(k_{\text{int}}a)\xi_l^{(1)'}(k_{ext}a) - \overline{n}\,\psi_l'(k_{\text{int}}a)\xi_l^{(1)}(k_{ext}a)}B_{lm} \tag{2.25.b}$$

$$c_{lm} = \frac{\xi_l^{(1)'}(k_{ext}a)\psi(k_{ext}a) - \xi_l^{(1)'}(k_{ext}a)\psi_l'(k_{ext}a)}{\overline{n}^2\psi_l(k_{\text{int}}a)\xi_l^{(1)'}(k_{ext}a) - \overline{n}\,\psi_l'(k_{\text{int}}a)\xi_l^{(1)}(k_{ext}a)}A_{lm} \tag{2.26.c}$$

$$d_{lm} = \frac{\xi_l^{(1)'}(k_{ext}a)\psi(k_{ext}a) - \xi_l^{(1)}(k_{ext}a)\psi_l'(k_{ext}a)}{\psi_l(k_{\text{int}}a)\xi_l^{(1)'}(k_{ext}a) - \bar{n}\,\psi_l'(k_{\text{int}}a)\xi_l^{(1)}(k_{ext}a)} B_{lm} \qquad (2.26.d)$$

where $\bar{n}$ is the complex relative refractive index $\bar{n} = (\bar{\varepsilon}/\varepsilon_{ext})^{1/2}$ and ξ is Ricatti-Bessel function.

For an arbitrary electromagnetic beam incident on a dielectric sphere, the calculation of internal and scattered electromagnetic beam starts from the calculation of A_{lm} and B_{lm} which describe the incident field are generated by the surface. Then the calculation results are combined to (2.25-2.26). This gives the most general series solution for the fields.

2.6.1 Absorbed Power and Modified Absorption Efficiency of a Dielectric Sphere

The time averaged absorbed power by the sphere can be obtained by integrating the radial component of Poynting vector over a spherical surface enclosing the surface[20]. The absorbed power is given as,

$$W_{abs} = -\frac{c}{8\pi} k_0^2 \varepsilon_{ext} \sum_{l=1}^{\infty} \sum_{m=-l}^{l} l(l+1)\left[\left|a_{lm}\right|^2 + \left|b_{lm}\right|^2 + \text{Re}(A_{lm}a_{lm}^* + B_{lm}b_{lm}^*)\right] \qquad (2.27)$$

Modified absorption efficiency is defined as the ratio of the total power absorbed by the sphere to the total power of the incident beam. Since the total power of the incident beam is $(c/16)E_0^2 w_0^2$ where E_0 is the electric field amplitude at the beam focus, multiplying reciprocal of this term by (2.27) gives us the modified absorption efficiency as;

$$\widetilde{Q}_{abs} = -\frac{2\alpha^2}{\pi \widetilde{w}_0^2 a^4 E_0^2} \sum_{l=1}^{\infty} \sum_{m=-l}^{m=l} l(l+1)\left[|a_{lm}|^2 + |b_{lm}|^2 + \mathrm{Re}(A_{lm} a_{lm}^* + B_{lm} b_{lm}^*) \right] \qquad (2.28)$$

2.6.2 Tightly Focused Gaussian Beam Case: Effects of focal Point Positioning

The calculation of optical modes from the scattering theory for a spherical, isotropic, homogenous sphere illuminated by a plane wave is best quantified by Mie theory. Since (2.25.a) and (2.25.b) show the transition from plane wave theory to arbitrary beam theory, structural resonances occur at the same size parameter for the illumination in both cases. However, experimental observations show us that focused Gaussian beam excites the modes of the sphere more efficiently than plane wave. For instance, for arbitrary beam illumination $2l$ circumferential peak cannot be observed where for plane-wave illumination this ring formation occurs. This is a consequence of single angular mode excitation by plane wave illumination. On the other hand, for arbitrary beam resonance case a series of angular modes ($-l \le m \le l$) can be excited. One of the main differences is the modified absorption efficiency. The modified absorption efficiency increases for TE resonance case, as the focal point of the beam is moved along x direction towards the surface as Fig 2.3.b and Fig 2.3.c. On the other hand, the modified absorption efficiency decreases drastically for the nonresonance and magnetic resonance case. For this case, the focal point of the beam is positioned away from the particle center[20].

The other reason is edge illumination. In the direction of the incident electric field polarization illumination, electric wave resonances are excited whereas for the edge illumination perpendicular to the direction of the incident electric field polarization only magnetic wave resonances are excited.

Electric and magnetic wave resonances are not excited for on-center focal point positioning. They can be excited on-edge focal point positioning.

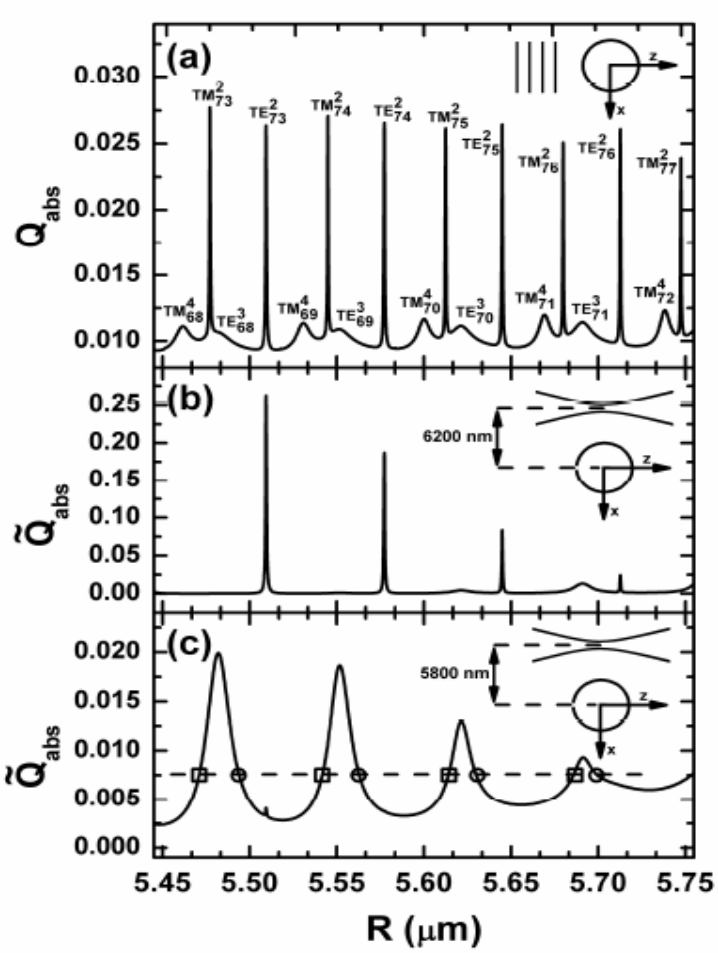

Figure 2. 3 Calculated absorption efficiency (Q_{abs}) and modified absorption efficiency ($\widetilde{Q}_{abs}$) as a function of radius (R) for a sphere having refractive index, $n = 1.33 + 4 \times 10^{-5} i$ (a) Plane wave illumination with transverse polarization. (b,c) Focused Gaussian beam illumination with linear polarization along x direction. Focus is positioned away from the center of the sphere along x direction at a distance of 6200 nm (b) and 5800 nm (c). All the waves propagate along z direction.

Chapter 3

OBSERVATION AND TUNABLITY OF WHISPERING GALLERY MODES FROM WATER MICRODROPLETS

3.1 Observation of WGMs from a Microdroplet

Water microdroplets have truncated spherical geometry when they are standing on a superhydrophobic surface. This nearly spherical geometry allows us to investigate them as microcavity. Collected WGMs from individual water microdroplets had quality factors more than 8000 when kept stable. The sensitivity of the resonances to the size and shape of the microdroplet reveals opportunities for the use of this technique as a probe to characterize superhydrophobic surfaces and investigate liquid-solid surfaces.

3.1.1 Experimental Setup

A home-built current controlled mini humidity chamber was used throughout the experiments as in Fig. 3.1. The chamber stood on the superhydrophobic surface, and an attached nebulizer generates microdroplets doped with 20 μM rhodamine B ranging from a few up to 30 μm in diameter as in Fig 3.2. WGMs were observed by the fluorescence spectrum collected from single microdroplets. High quality and low volume WGMs

enhance the rhodamine B emission at resonant wavelengths, hence enabling their observation. Joule heating of a 3 Ω nichrome wire resistor was used to control the ambient humidity level of the chamber, causing evaporation or condensation in microdroplets. Heating currents between 0.15 and 0.3 A were used to obtain stable or nearly stable microdroplets. Although the stabilizing heating current was not constant between the experiments, fine tuning with 0.01A sensitivity helped to keep the size of the microdroplets highly stable. Additional parameter for local stability control was laser power absorbed by microdroplets [10].

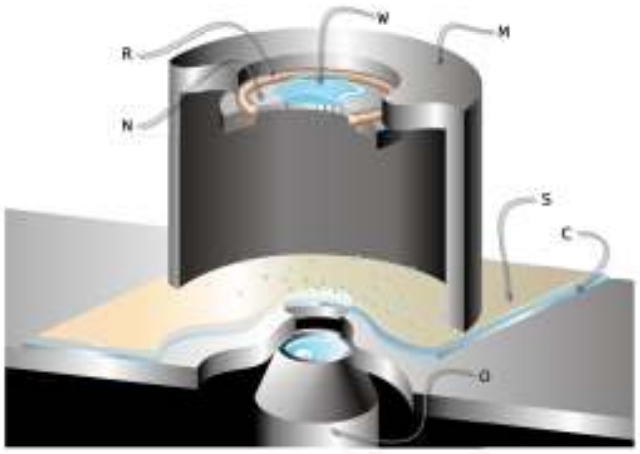

Figure 3. 1 Illustration of the experimental setup. N, ultrasonic nebulizer; R, nichrome resistor; W, reservoir of rhodamine B doped water; M, mini chamber; S, superhydrophobic surface; C, cover glass; O, microscope objective

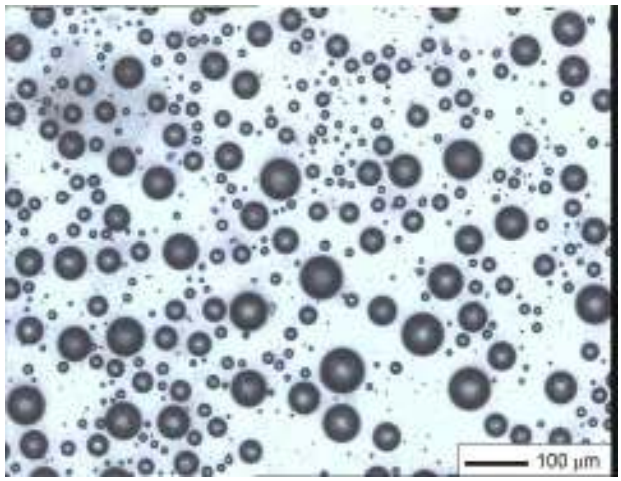

Figure 3. 2 Top view of water microdroplets on the superhydrophobic surface.

A continuous wave solid-state laser $\lambda = 532nm$ was used to excite the microdroplets within resolution limited spots near the outer surface. Excitation of microdroplets and collection of the fluorescence were done through a high numerical aperture microscope objective (60×, NA=1.4) in the inverted geometry. After being transmitted through a dichroic mirror (Q570LP), and a 1.5× magnifier element, the collected fluorescence was dispersed using a 50 cm monochromator (spectral resolution of 0.06 nm) and detected by a charge coupled device camera. All the emission spectra presented in this letter were taken using an exposure time of 2 s, under excitation intensities between 2 and 5 μW. Each exposure of the camera was followed by 2.14 s readout time [10].

3.1.2 Characterization of WGM from a Stable Microdroplet

Fig 3.3 and 3.4 show high resolution spectra obtained from a sizewise stable microdroplet. The temporal stability and the integrated spectrum of the microcavity is demonstrated in the contour plot fig 3.3. During 82.8 s of data acquisition no spectral drift was observed in the WGMs within the resolution of the spectrometer setup (0.06 nm). This corresponds to a size stability of 1 nm. The decrease in the intensity of the WGMs between consecutive acquisitions was due to photobleaching of rhodamine B molecules, fig 3.4. Under the assumption of a dielectric sphere in air, the observed WGMs are identified by two linearly independent solutions to the Helmholtz equation with a mode number n and mode order l ($TE_{n,l}$ and $TM_{n,l}$ WGMs)[34]. For the spectra shown in Fig. 3.3, we identified the WGMs located at 583.85 and 587.17 nm as WGM A and WGM B with mode order 1 respectively. The peak at 585.90 nm with a relatively large full width at half maximum (FWHM) should stem from a WGM with a high mode order. In the low pumping regime where stimulated emission is negligible as compared to spontaneous emission, the quality factors (Q factors) of the WGMs are given by the FWHMs of the observed peaks. This condition was satisfied in our experiments with the selected excitation intensity (2–5 μW), which was much smaller than the saturation power of the 20 μM rhodamine B solution. In Fig. 3.3 a Q factor of 3400 was observed for the peak at 585.90 nm, while the Q factors of the WGM A and WGM B were determined to be larger than 8000, which is almost the resolution limit of our experimental setup. Considering the microdroplet radius of 7 μm, the free spectral range (FSR) of the WGMs is expected to be larger than 7 nm[35] yielding a minimum finesse (FSR/FWHM) of ~100 for the high quality WGMs [10].

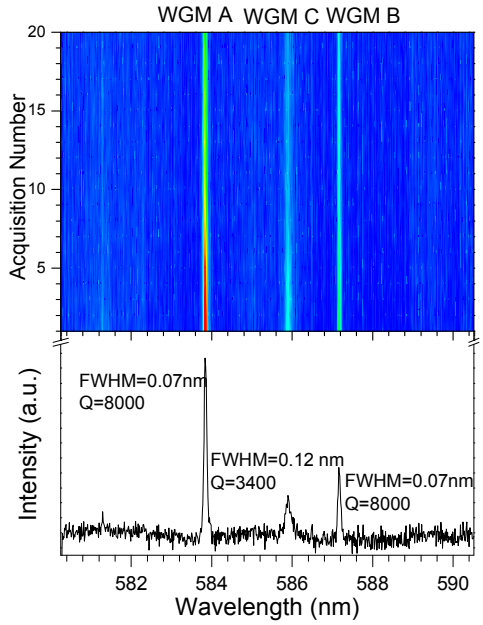

Figure 3. 3 Top figure: Contour plot of the emission spectra taken from a microdroplet with a radius of 6 μm showing stable WGMs. Intensity values in arbitrary units increase from blue to red. Below: Sum of the 20 acquisitions in. The peaks at 583.85 and 587.17 nm are identified as WGM A and WGM B, respectively.

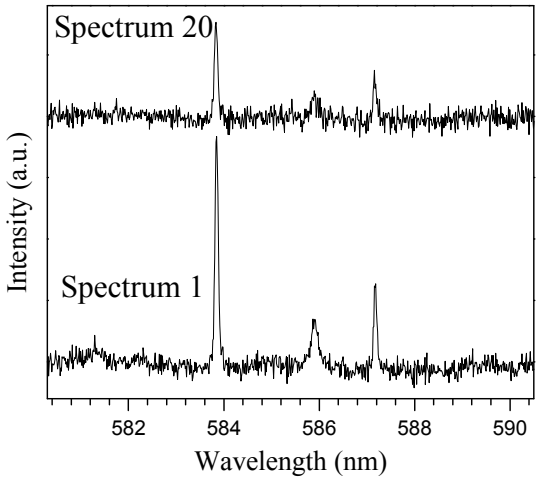

Figure 3. 4 Photobleaching of Rhodamine B molecules after 20 data acquisitions.

Proof of negligible stimulated emission is also evident in the acquired high resolution spectra. Relative intensities of the three WGMs in Fig. 3.3 were preserved during the acquisitions despite significant photobleaching. Hence no lasing threshold was observed between the corresponding acquisitions. The fact that the low quality WGM had intensity comparable to the intensities of the two high quality WGMs is another evidence for the absence of lasing. The lasing modes should be redshifted, which we did not observe[36], [10].

3.1.3 Free Spectral Range of the Collected Modes

For an ideal sphere with a large structural factor ($x = 2\pi a / \lambda$), FSR is inversely proportional to the radius, a [35]. Figure 3.5 depicts the dependence of the observed FSRs as a function of the reciprocal radii of microdroplets. For each measured FSR, the radius of

the microdroplet was determined from fluorescence optical images as seen in the inset in Fig. 3.5. The revealed linearity between FSR and $1/a$ is an indication of the nearly spherical geometry of the microdroplets. The difference between the best fit to experimental data (solid line) and the expected radius dependence for ideal water microspheres in air (dashed line) reflects[35] the deviation from an ideal sphere to a truncated spherical shape on the superhydrophobic surface.

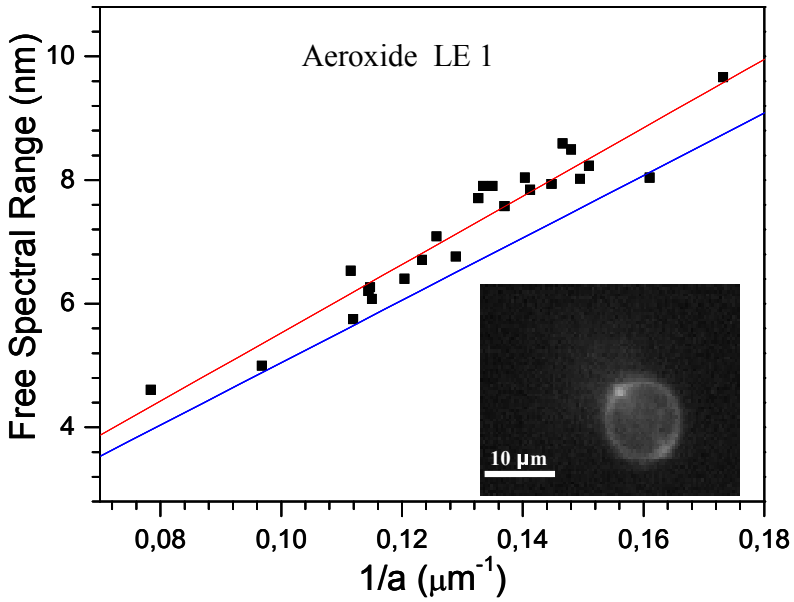

Figure 3. 5 (a) FSR of WGMs as a function of the reciprocal radii of the microdroplets. The dashed line is the expected dependence for ideal water microspheres in air. The solid line is the best fit to the experimental data. The linear dependence reflects nearly spherical geometry of the water microdroplets. (b) Fluorescence image of a water microdroplet. Characteristic ring shape of the WGMs is visible

3.1.4 Free Spectral Calculation for Different Aeroxides

As stated in section 1.2, LE1 and LE2 have different characteristics due to surface roughness. Different FSR of WGMs has obtained from different water microdroplets doped with Rhodamine B dye molecules and glycerol standing on LE1 and LE2 coated substrate as in fig 3.6 and 3.7 respectively. Due to the absence of the humidity chamber, determining rhodamine B and glycerol concentrations in the remained droplet is difficult. Considering sudden evaporation and increase in the doped materials, the best fit experimental data will be anticipated to have totally different slope than in figure 3.6 and 3.7.

During the experiments, it was realized that WGMs were easily collected from LE2 coated surfaces. This is interpreted as for smaller sized microdroplets, the contact angle of the droplets are larger than of droplets with the same size on LE1 due to surface roughness

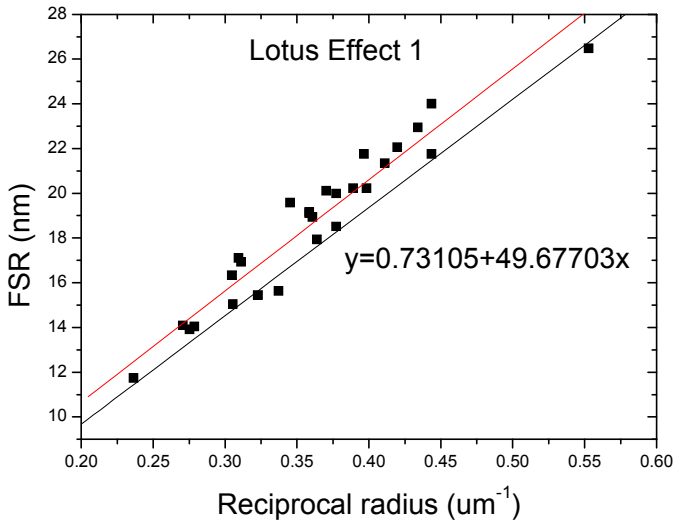

Figure 3. 6 FSR versus reciprocal radii for microdroplets on LE1 surface

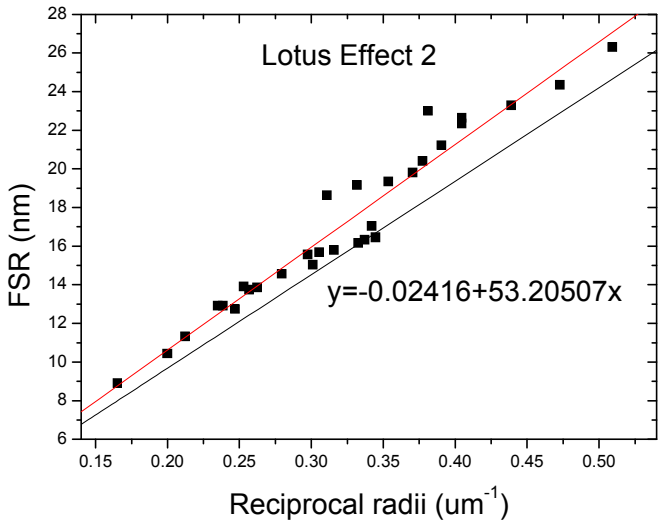

Figure 3. 7 FSR versus reciprocal radii for microdroplets on LE2 surface The redline shows the best fit experimental data whereas the blue line shows a dielectric sphere in air

3.2 Tunability of WGM

Applications of optical microcavities in optical communication systems based on wavelength division multiplexing have been demonstrated by various studies using semiconductor or polymer microdisk and microring microcavities. Despite the inherent potential, microcavity based devices have not found wide use in modern optoelectronic networks. One of the main obstacles has been tunability. Refractive index control of the constituent materials in a solid microcavity by changing the temperature or the electric field applied to liquid crystal cladding layers enabled limited tunability within a maximum spectral range of 0.25 nm. Controlling size and shape an alternative mechanism for tuning

microcavity resonances. Using solid optical microcavities a maximum tunability of 1 nm was demonstrated under a large external force [37]. In contrast, a liquid microcavity provides relatively easy control of its shape due to its viscous nature. An applied external force, electric field, or control of the evaporation/condensation kinetics can induce size and shape changes in liquids. Liquid lenses, in which electrical field is used to control the shape, have even found technological applications[11].

3.3 Tunability of WGMs Collected From a Water Microdroplet Standing on the Surface

WGMs were tuned in the directions of both evaporation and condensation as a function of the ambient humidity. Figure 3.8 through 3.10 show the consecutive spectra taken from three different microdroplets. Evaporation was observed in Fig. 3.8 leading to a total spectral drift of 3.1 nm, whereas in Fig. 3.9 condensation caused a total spectral drift of 9.6 nm in the WGMs. In Fig. 3.10, the direction of evaporation was reversed by the sudden increase of local humidity as a result of an increase in the heating current from 0.28 to 0.31 A. After a spectral drift by 2.6 nm in the direction of evaporation, a spectral drift of 3.3 nm was observed in the direction of condensation [10].

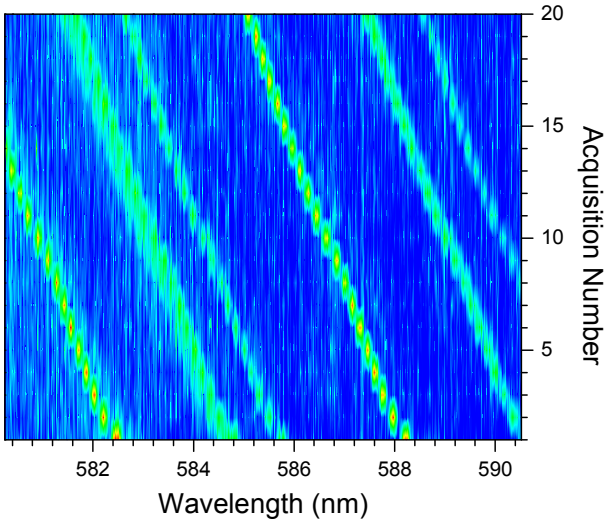

Figure 3. 8 Consecutive spectra taken from a microdroplet exhibiting evaporation, total spectral drift 3.1 nm observed

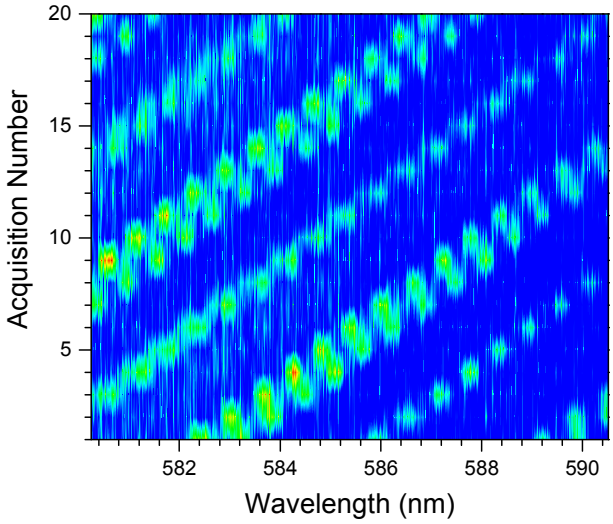

Figure 3. 9 Consecutive spectra taken from a microdroplet exhibiting condensation, total spectral drift 9.6 nm observed

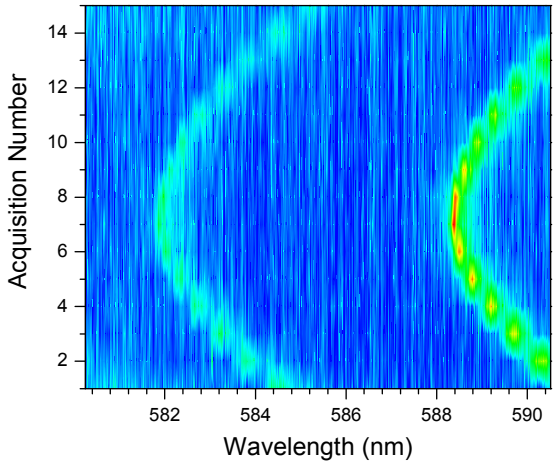

Figure 3. 10 Consecutive spectra taken from a microdroplet exhibiting first evaporation with a total spectral drift 2.6 nm then condensation with total spectral drift 3.3 nm observed

3.4 The Effects of Electric Field on Droplet Geometry

The shape of a water microdroplet on the surface is determined by the surface energy of solid and the composition of the liquid (ionic, solvent) [38]. When external electric field is applied to the droplet, redistribution of the ions and dipoles change its shape [39]. In these experiments, superhydrophobic coating was applied to indium tin oxide (ITO) coated cover glasses (Figure 3.11). For a millimeter sized water droplet, the electric field is applied by inserting a needle inside the droplet (Figure 3.12.a). It is evident in Figure 3.12, increasing electric field causes to a decrease in contact angle because of large shape deformation (Figure 3.13).

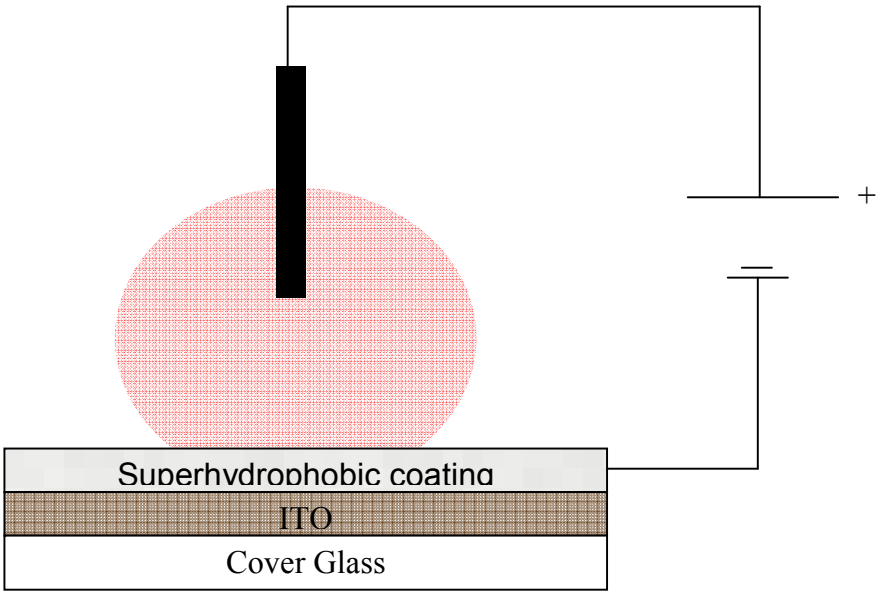

Figure 3. 11 Schematic diagram of electrowetting set-up

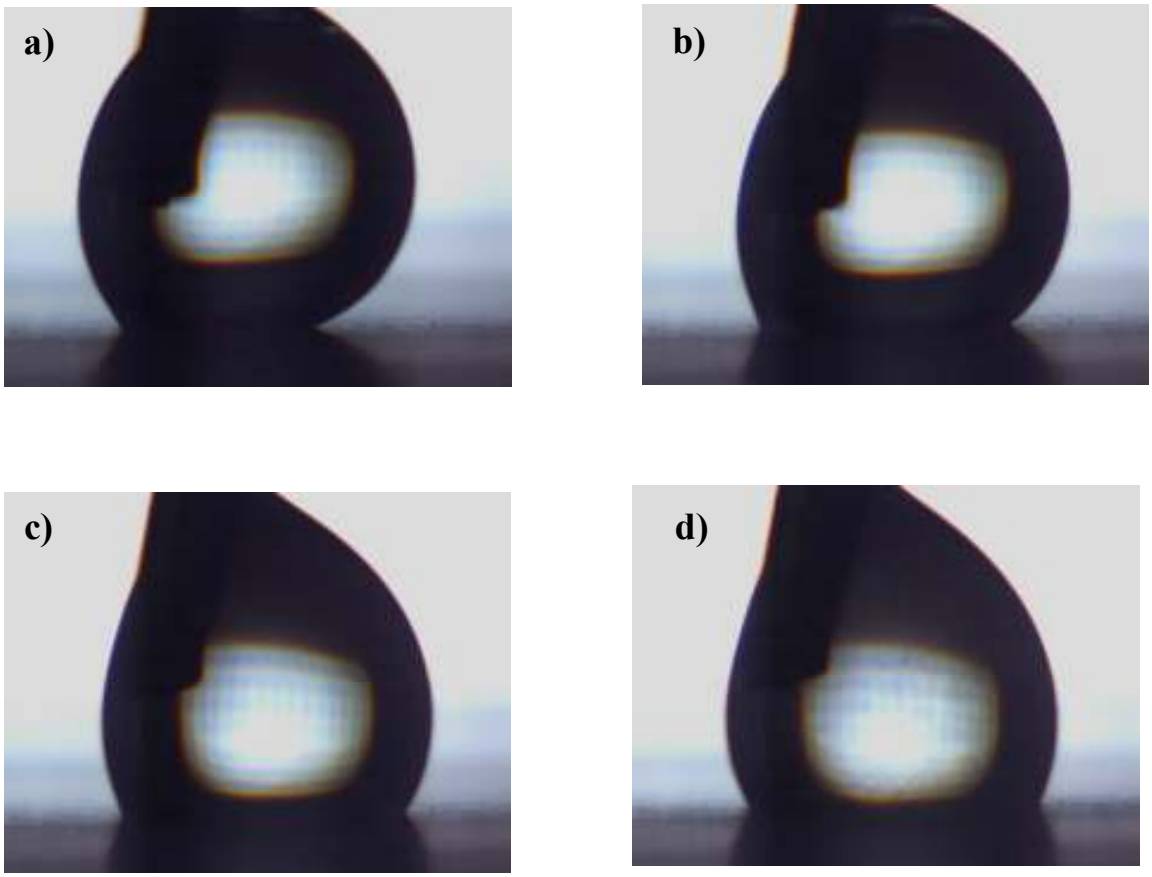

Figure 3. 12 The change in shape under an applied DC electric field for a water droplet. a) The right contact angle is about 154^0 when voltage is 0 V, b) the contact angle is 146^0 voltage is 100 V, c) the contact angle is 125^0 voltage is 220 V, d) the contact angle is 109^0 voltage is 330V

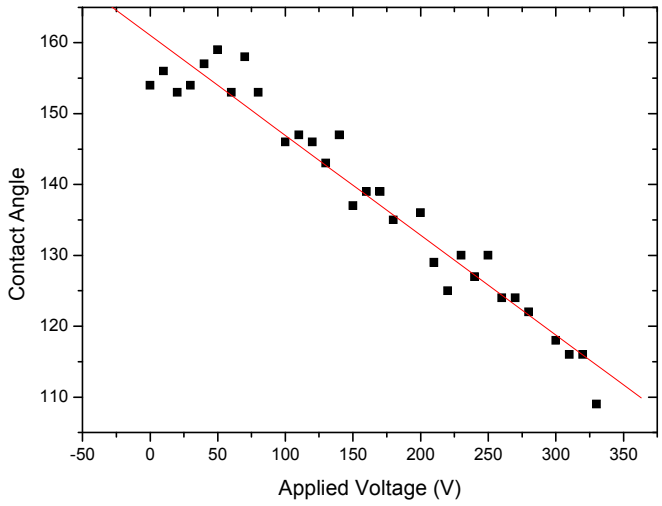

Figure 3. 13 The change in contact angle of a millimeter size water microdroplet under DC electric field

The observed change in shape under external field leads us to investigate tunability of WGMs of a microdroplet. The dependence of the change in the average contact angle with applied external electric field for a micrometer sized 5 μM Rhodamine B doped glycerol/water microdroplet is given in Figure 3.14. Even though no significant mode shifts observed, the FWHM of the collected modes are getting larger as we increase applied voltage from 0 V to 400 V (Figure 3.14 (a), (b) and (c)). Probably, this is a consequence of the vibrations of the microdroplet under electric field. When we decrease the applied electric field the wide FWHM becomes narrower as in Figure 3.14 (d) and (e). This reversibility of FWHM is also an evidence for the vibrations.

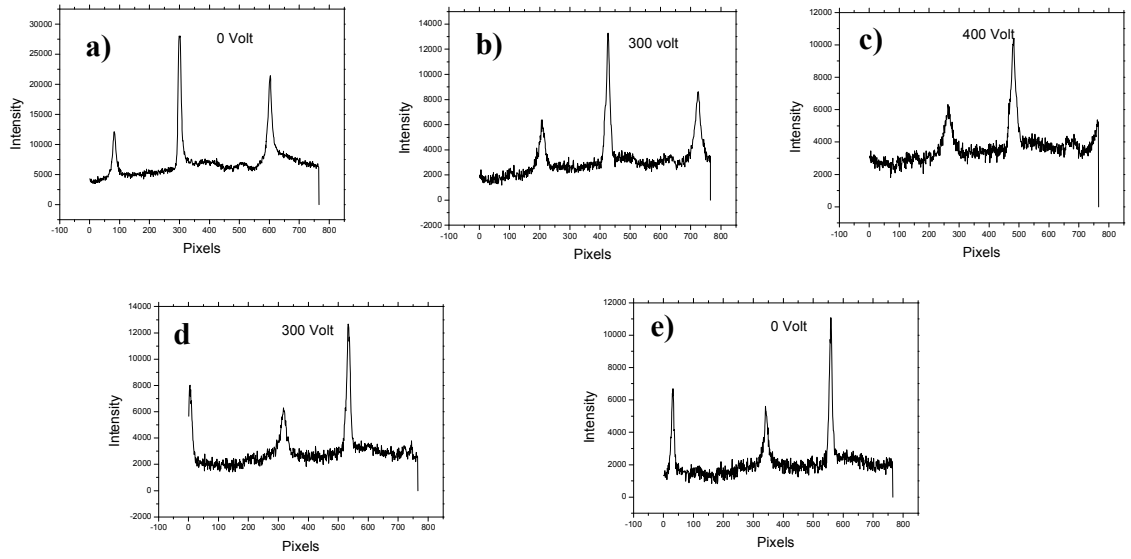

Figure 3. 14 The spectrum of a glycerol/water microdroplet under applied DC voltage of a) 0 V, b) 300, c) 400 V, d) 300 V, e) 0 V

3.5 Summary

In this work a water microdroplet resting on a superhydrophobic surface was introduced as a largely tunable optical microcavity. For future applications, faster tuning methods can be developed with an applied external force or electric field[40]. Enhancement of optical field intensities in the water microcavity might lead to applications in fluid sensing or precise measurements of optical interactions in minute samples of biological specimens or biomolecules. The measurement technique presented here can also serve as a useful probe in characterizing the dynamics at liquid/solid interfaces due to its high sensitivity to the size and shape of microdroplets.

Chapter 4

VOLUME STABILIZATION OF SINGLE DYE-DOPED WATER MICRODROPLETS WITH FEMTOLITER RESOLUTION

4.1 Introduction

With their almost spherical geometries and smooth surfaces, liquid microdroplets are naturally attractive to function as optical microcavities. They host high quality whispering gallery modes (WGMs) which inspired various applications in areas as: laser diagnostics [35],[36] atmospheric science, biology, and interfacial chemistry. Size control has been an important challenge in applications using microdroplets of liquids with relatively high vapor pressures. This hindered detailed studies of the dynamics at specific gas-liquid interfaces. Only very recently single water microdroplets were analyzed for long time periods [41],[42]. In these experiments, microdroplets with initial salt concentrations between 0.04-1.28 M reached to a stable volume by evaporation in a humidity controlled chamber.

Sudden evaporation and condensation of water microdroplets depend on two parameters during our experiments. One is the level of the ambient humidity inside the humidity chamber [10]. In previous chapter, it is stated that the level of the ambient humidity is changed by the current passing through the wire resistor. During the conduction of the experiments, if a droplet exhibits sudden evaporation or condensation, by

changing the level of the current, we could stabilize it. On the other hand, some microdroplets which are exhibiting condensation or evaporation could stabilize its volume explained by the size dependent absorption phenomena.

We demonstrated a self control mechanism that stabilizes the size of Rhodamine B-doped water microdroplets standing on a superhydrophobic surface. The mechanism relies on the interplay between the condensation rate that was kept constant and evaporation rate induced by laser excitation which critically depends on the size of the microdroplets. The radii of individual water microdroplets (>5 μm) stayed within a few nanometers during long time periods (up to 455 seconds). By blocking the laser excitation for 500 msec, the stable volume of individual microdroplets was shown to change stepwise.

4.2 Size Dependent Absorption Phenomena

Size dependent absorption phenomenon plays a crucial role in the realization of the reported high precision volume stabilization mechanism. Figure 4.1 shows the calculated absorption efficiency (Q_{abs}) and modified absorption efficiency $(\widetilde{Q}_{abs})$ as a function of radius (R) for a sphere having a refractive index equal to that of 50 μM Rhodamine B-doped water $(n = 1.33 + 4.\times 10^{-5} i)$. In Fig.4.1 (a), calculation results are presented for a plane wave excitation (λ = 532 nm, transverse polarized), where TE and TM modes appear. Fig.4.1 (b) and (c) simulate our experiment, with a tightly focused Gaussian beam (λ = 532 nm, ω_0 = 250 nm, linearly polarized along the x direction), and were calculated using the localized model developed by Gouesbet et al.[43] with an algorithm introduced by Lock[44] . (Q_{abs}) and $(\widetilde{Q}_{abs})$ are the ratios of the total power absorbed by the sphere to the power incident upon the projected area of the sphere and to the total power of the

incident beam respectively as described in chapter 1. In Fig. 4.1(a) the first order modes are suppressed due to the high absorption coefficient [24]. In Fig.s 4.1(b) and 4.1(c) the focal points are located at 6200 nm and 5800 nm (off axis illumination) respectively. In these figures only the TE modes are excited as a result of the polarization direction. As the excitation spot approaches to the surface of the sphere, absorption of the lower-quality third orders modes dominate over the absorption of the second order modes (The algorithm can be found in Appendix A).

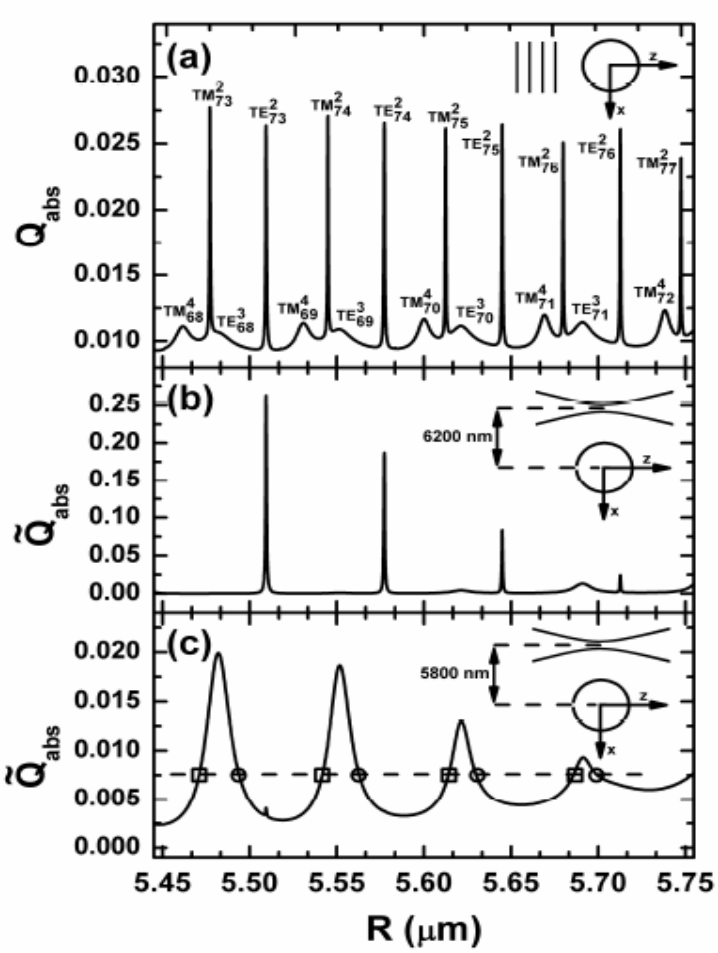

Figure 4. 1 Calculated absorption efficiency (Q_{abs}) and modified absorption efficiency ($\tilde{Q}_{abs}$) as a function of radius (R) for a sphere having refractive index ($n = 1.33 + 4.\times 10^{-5} i$). (a) Plane wave illumination with transverse polarization. (b,c) Focused Gaussian beam illumination with linear polarization along x direction. Focus is positioned away from the center of the sphere along x direction at a distance of 6200 nm (b) and 5800 nm (c). All the waves propagate along z direction.

The size of the microdroplet is determined by the balance between the condensations rate Γ_{cond}, and the evaporation rate Γ_{evap}. In our experiments, Γ_{cond} was kept

at a constant value as indicated by the dashed line in Fig. 4.1c. Γ_{evap} was proportional Q_{abs} ($\Gamma_{evap} \propto IQ_{abs}$), ($I$ laser intensity) and changed with the size of microdroplet as it shrunk ($\Gamma_{cond} < \Gamma_{evap}$) or grew ($\Gamma_{cond} > \Gamma_{evap}$) in size. For each WGM, the microdroplet can be at equilibrium at two different sizes as indicated by a solid square on the left of the peak and a solid circle on the right. The square corresponds to a stable equilibrium point where a self-locking mechanism is in effect: an increase in size due to condensation or a decrease in size due to evaporation is counterbalanced by a corresponding increase or decrease, respectively, in $\widetilde{Q}_{abs}$ maintaining the equality. On the contrary, the circle corresponds to an unstable equilibrium: an increase in size causes $\widetilde{Q}_{abs}$ to decrease and the microdroplet continues growing in size. Similarly, a decrease in size causes $\widetilde{Q}_{abs}$ to increase and the microdroplet continues shrinking in size.

4.3 Volume Stabilization by Laser Absorption

We demonstrated a volume stabilization of a microdroplet which was exhibiting condensation by laser absorption phenomena. By the size dependent laser absorption phenomena, as it gets higher radius, at some value of radius, $\widetilde{Q}_{abs}$ will cause self stabilization by my making the condensation rate equal to evaporation rate (solid square). Fig. 4.2 shows the contour plot of consecutive fluorescent spectra taken from individual microdroplet (radius of 5.7 μm before the first acquisition) exhibiting volume stabilization. In all contour plots in this report, the intensity variation is given and constant Rhodamine B emission is taken to be zero. At acquisition 16, Γ_{cond} equals to Γ_{evap} at a stable equilibrium point, initiating the stabilization mechanism. Starting at this point, despite any change in

the ambient humidity, the three WGMs stop drifting and remain stable within a full width at half maximum (FWHM) of 0.13 nm until the end of the experimental period. The observed spectral linewidth of 0.13 nm corresponds to a volume stabilization within 0.53 fl (radius stabilization of 1.3 nm) over the course of the experiment (455 seconds). In this experiment, the microdroplet was excited in the very vicinity of its rim as shown in the inset of Fig. 4.2. However, experimental setup was unable to point the exact location of the laser focus, which demands higher spatial resolution.

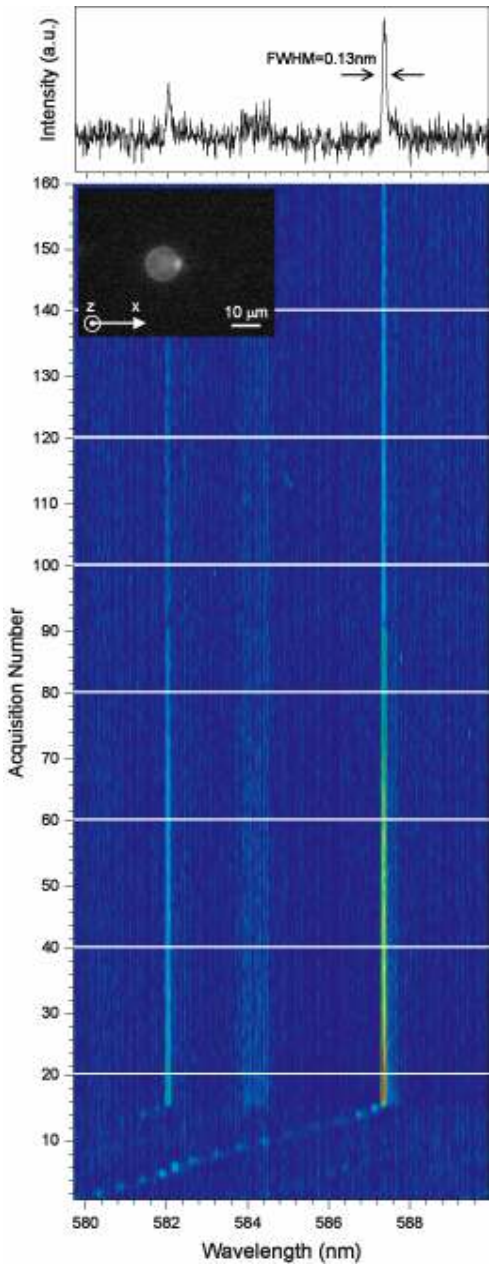

Figure 4. 2 Volume stabilization by laser absorption. Microdroplet is first exhibiting condensation then it exhibits stabilization

4.4 Effects of a Laser Beam Blocking on WGMs of a Stable Microdroplet

By blocking the laser for short time intervals, the stable volume of a microdroplet can be changed stepwise. This is demonstrated in Fig. 4.3 where laser beam is blocked for 500 ms before acquisitions 10, 20, 30, 50, and 68. Each interim laser blocking causes the WGMs to start drifting to larger wavelengths. The microdroplet volume then stabilizes at consecutive stable equilibrium points. Accurate identifications of the polarization, mode numbers (n), and orders (r) of the WGMs are omitted in Fig. 4.3 and others to avoid errors caused by nonspherical microdroplet geometry. Radius of this microdroplet is determined to be 5.4 μm from the fluorescence image before the first acquisition. An almost constant spectral drift of 11 nm is observed between consecutive stable equilibrium points. Assuming an ideal spherical geometry, this corresponds to an increase in the radius of this microdroplet by 102 nm. This implies a volume step of 37 fl. Here we consider that the most intense WGMs observed in the emission spectra have mode orders of 1 (TE or TM polarized). These spectral observations do not allow for an accurate assignment of the WGMs absorbing at λ = 532 nm. Should the absorbing WGMs be of mode orders 2 or 3, spectral steps of 7.3 nm (7.4 nm) or 7.5~nm (7.5~nm) would be observed in the first order TE (TM) WGMs in the emission spectra. These values are still largely different than the observed 11 nm spectral step, mainly due to the characteristic geometry of the microdroplets on a superhydrophobic surface.

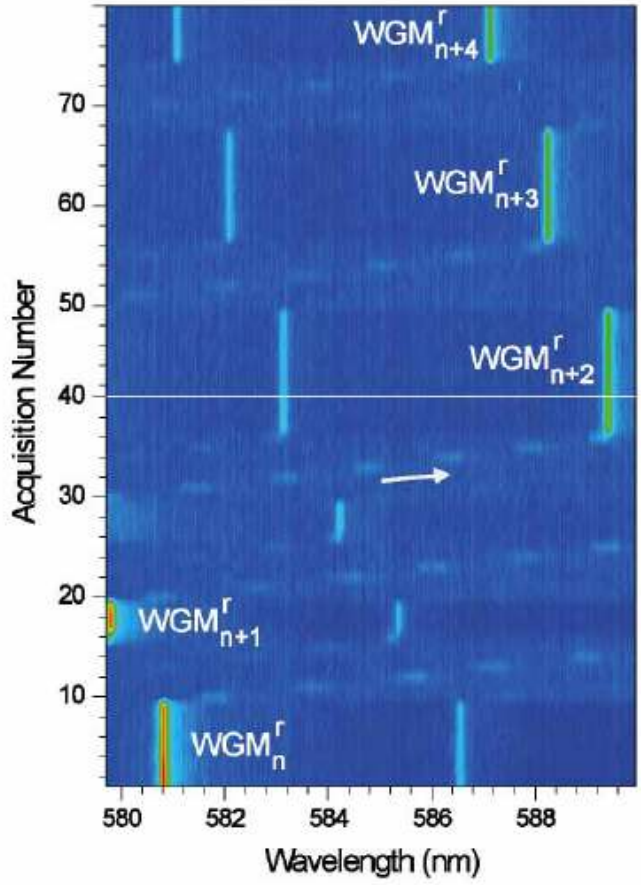

Figure 4. 3 Effects of laser beam blocking on WGMs of 5.4 μm radius droplet

4.5 Effects of Evaporation and Condensation Rate on WGMs of Microdroplets

In addition to volume stabilization, two operation regimes can be observed. If Γ_{cond} is smaller than Γ_{evap} for any given radius, evaporation is observed in the microdroplet. For this

case, the microdroplet will evaporate at an almost constant rate until the laser reaches the spectral vicinity of a WGM. When the laser resonates with a WGM, an increase in local heating will follow the enhanced laser absorption. This will result with an increase in the rate of microdroplet shrinking as observed in acquisitions 18 and 19 in Fig. 4.4 (a).

When Γ_{cond} is larger than Γ_{evap} for all radii of a given microdroplet, it will keep growing in size as shown in Fig. 4.4 (b) (WGMs drift at a rate of 0.93 nm/acquisition). Both the relatively large Γ_{cond}, and the position of the focal spot relative to the microdroplet play roles in preventing the onset of volume stabilization in Fig. 4.4(b). Volume stabilization is observed when the laser intensity is increased from 2.5 μW to 3.0 μW as seen between acquisitions 1-5 in Fig. 4.6. After the interim laser blocking for 500 ms before acquisition 6, WGMs start drifting at a rate of 0.63 nm/acquisition between acquisitions 6-13. The rate at which the size of this microdroplet grows is largely reduced between acquisitions 14-15, resulting in no spectral drift in WGMs within the spectral resolution of the experimental setup. However volume stabilization is not established at the end of acquisition 15. WGMs drift at a rate of 0.65 nm/acquisition between acquisitions 16-30.

Selections of a proper liquid and laser intensity are decisive in achieving volume stabilization using the scheme described. Liquid's physical properties come into play in relating the laser induced heating to the evaporation rate of the microdroplet. Such a detailed analysis requires the solution of the heat transfer over the three-dimensional geometry of the microdroplet. Nevertheless, our experiments revealed that 50 μM Rhodamine B-doped water microdroplets reflect the changes in the local heating to the microdroplet growing rate with high sensitivity. This is eminent in the strong laser intensity dependence of the drift rate of WGMs in Fig.s 4.4 (b) and 4.4 (c).

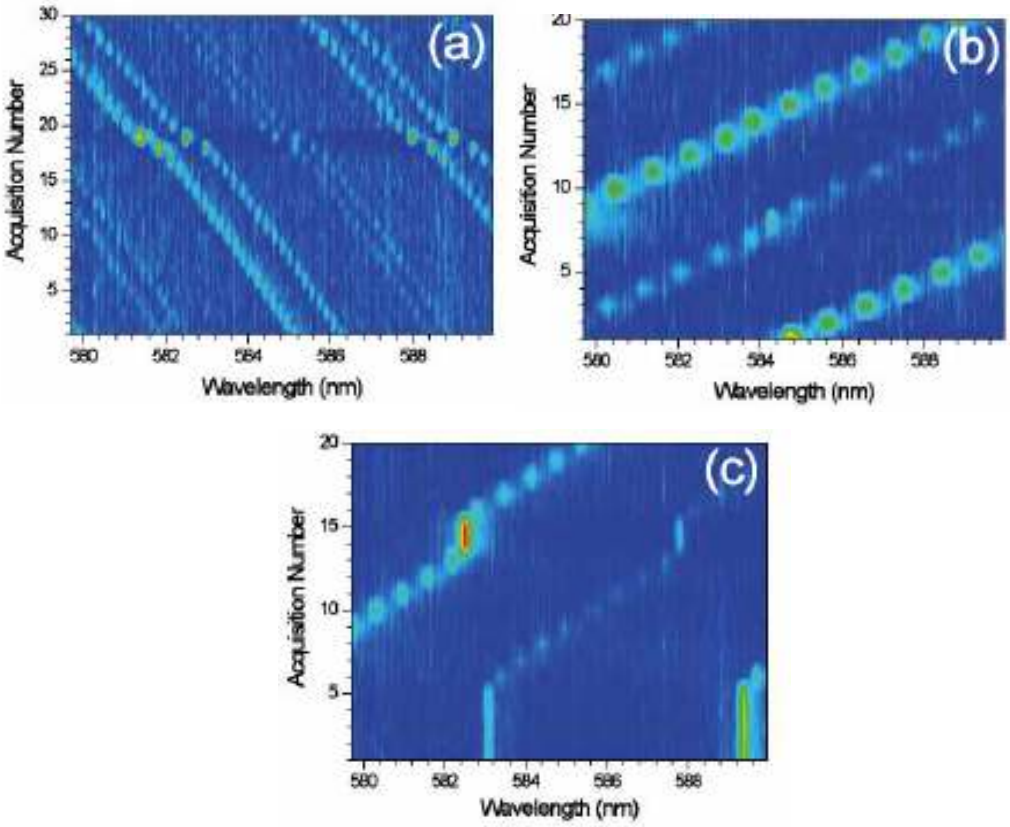

Figure 4. 4 (a) Contour plot of emission spectra from a continuously shrinking microdroplet. Radius of the microdroplet is 8.9 μm before acquisition 1. Excitation intensity is 1.9 μW. Focus is positioned in the vicinity of the rim away from the center along x direction. (b,c) Contour plots of emission spectra from a microdroplet growing continuously in size. Radius is determined to be 5.2 μm before acquisition 1 in (b). Focus is positioned away from the center along x direction at a distance of 2.6 μm. Excitation intensities are 2.5 μW and 3.0 μW in (b) and (c) respectively. Intensity values in arbitrary units increase from blue to red.

4.6 Summary

In this chapter we demonstrated a self control mechanism that stabilizes water microdroplets by size dependent laser absorption. Though we have routinely achieved volume stabilization, the maximum time during which stabilization was observed did not exceed 455 seconds in our experiments. This is mainly due to photobleaching of Rhodamine B molecules. The corresponding change in the absorption coefficient often resulted in the loss of volume stabilization, typically after several minutes. We envision that using more photostable dye molecules or chemically synthesized quantum dots, the maximum volume stabilization time could be drastically improved.

Chapter 5

LASING FROM SINGLE, STATIONARY DYE-DOPED GLYCEROL/WATER MICRODROPLETS

5.1 Introduction

Optical microcavities are attractive in the development of ultralow-threshold lasers because they can confine high-quality optical resonances in small volumes [11]. Such light sources hold a great promise for applications in optical communications systems and fundamental studies in cavity quantum electrodynamics. Up to date, laser emission has been observed from various different optical microcavities based on semiconductors or polymers. Examples include microdisks [45], microspheres [12], micropillars [46], and photonic crystal defect microcavities [9].

Observation of laser emission from liquid microdroplets flying in air have been demonstrated for 20 years [47]. In these experiments, a stream of dye-doped ethanol droplets was excited by a pulsed laser. Laser action was observed by analyzing the emission spectra collected from single microdroplets excited by single pump pulses. To date, however, lasing from stationary microdroplets has not been reported. One challenge in this case stems from the fact that the physical characteristics of the surface need to be carefully optimized in order to minimize the geometric deformation of the otherwise spherical droplet and to maintain a sufficiently high quality factor for the resonant modes [48].

In this chapter, we demonstrate laser emission from single, stationary, dye-doped glycerol/water microdroplets located on a superhydrophobic surface. Due to the superhydrophobic nature of the surface, the spherical structure of the droplets is well maintained and a mode structure similar to that of an ideal spherical resonator can be obtained [10]. Furthermore, in contrast to the previous demonstrations, the technique used allows for the analysis of laser emission from a particular microdroplet over prolonged periods[48].

5.2 Dye Molecules as the Active Medium

The laser medium is the region in which stimulated emission occurs. Dye lasers use organic dyes as active medium which are dissolved in liquids such as water, ethyl alcohol or glycerol. The dye-doped liquid medium has advantages over solids or gases: They are easily available, easier to cool down and they can reach higher densities than gas lasers. In our experiments, we used Rhodamine B dye molecules which were diluted in a glycerol-water mixture. Rhodamine B dye molecules are in Xanthene dye family whose laser emission is in the visible range. Figure 5.1 shows the molecular structure of Rhodamine B.

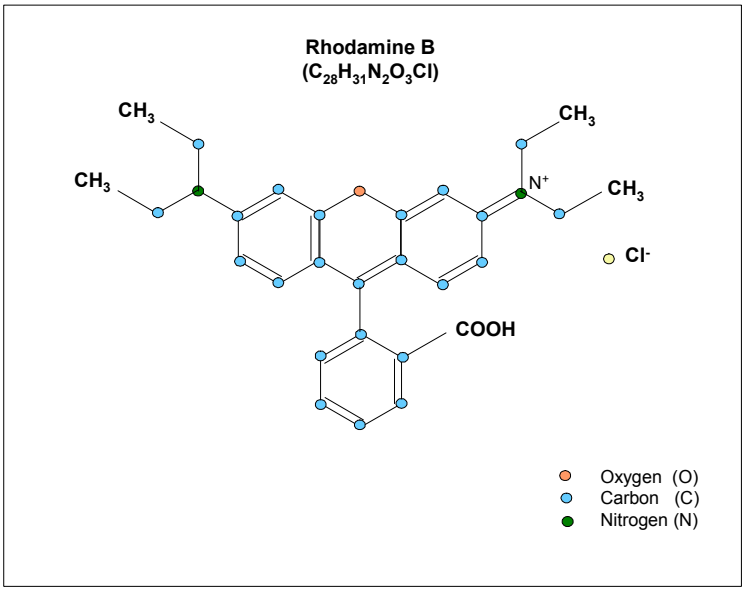

Figure 5. 1 Molecular structure of Rhodamine B

Organic dyes usually show wide absorption and fluorescence bands without sharp features as shown in figure 1.2 and figure 1.3. The fluorescence band is Stokes-shifted to longer wavelengths compared to absorption. Dye lasers are therefore attractive as tunable lasers over a relatively wide spectrum.

5.3 The Four Level System

In 1917 Einstein discussed the interaction of electromagnetic radiation with atoms [49]. He postulated three forms of energy exchange: absorption, stimulated absorption and stimulated emission. The formalism which was introduced by Einstein is well suited to explain lasing in a cavity containing dye molecules as the active medium.

Here, we consider a four-level system to dicuss the process in the lasing medium. Four level system consists of four energy levels in which level 1 is considered as ground state and 2, 3, 4 are excited states as shown in Figure 5.2. Atoms in the ground state are excited to the fourth level by a pump laser. Level 4 could consist of a large number of levels or could be a broad level. These excited atoms rapidly decay (typically <10 ps) to level 3 via nonradiative transition. Level 3 is the upper laser level and it has a long lifetime (typically 3-10 ns). The stimulated emission occurs when atoms in level 3 decay to level 2 where level 2 is considered as lower laser level. If level 2 has a very short time, atoms coming from level 3 can immediately relax down to level 1 and hence population inversion between 3 and 2 is maintained.

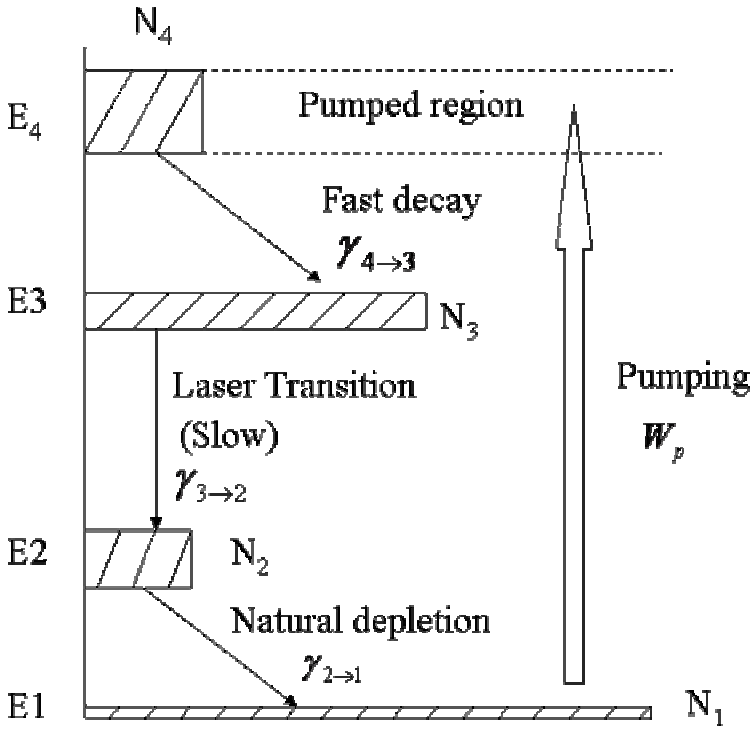

Figure 5. 2 The Four Level System

For a four level system the mathematical formalism of the rate equations is similar to the formalism used for a three level system [50]. Let N_1, N_2, N_3, N_4 represent the population density of the levels 1, 2, 3, 4 respectively. The change in the populations in level 4 is obtained as;

$$\frac{dN_4}{dt} = W_p(N_1 - N_4) - \frac{1}{\tau_4}N_4 \tag{5.1}$$

In the above equation $W_p(N_1 - N_4)$ represents the net rate of stimulated absorption between level 1 and level 4 by the pump. The first term describes the rate at which atoms are being pumped from the ground level. Not all atoms decay to level 3. Some of them decay to level 2 and level 1. Therefore the lifetime τ_4 is given as;

$$\frac{1}{\tau_4} = \gamma_4 = \gamma_{4\to3} + \gamma_{4\to2} + \gamma_{4\to1} \tag{5.2}$$

Similarly when atoms are relaxed down to level 3, some of them will decay to level 2 and others to level 1. Then the rate equation for N_3 can be written as

$$\frac{dN_3}{dt} = \gamma_{4\to3}N_4 - \gamma_3 N_3 = \frac{N_4}{\tau_{4\to3}} - \frac{N_3}{\tau_3} \tag{5.3}$$

where $\gamma_3 = \gamma_{3\to2} + \gamma_{3\to1}$. The third term represents the rate of loss of atoms from level 3 to levels 2 and 1 through spontaneous emission.

The rate equation for N_2 is obtained as;

$$\frac{dN_2}{dt} = \gamma_{4\to2}N_4 - \gamma_{2\to1}N_2 + \gamma_{3\to2}N_3 = \frac{N_4}{\tau_{4\to2}} + \frac{N_3}{\tau_{3\to2}} - \frac{N_2}{\tau_{2\to1}} \tag{5.4}$$

The first and the last terms in (5.4) show the relaxation rates of the atoms decaying from level 4 and level 3.

The rate equation for N_1 is obtained as;

$$\frac{dN_1}{dt} = W_p(N_4 - N_1) + \gamma_{4\to1}N_4 + \gamma_{3\to1}N_3 + \gamma_{2\to1}N_2 \tag{5.5}$$

At the steady states the term on the left hand side of equations 5.1, 5.3, 5.4, 5.5 equal to zero. From this point, equation 5.3 becomes as;

$$N_3 = \frac{\tau_3}{\tau_{4\to3}} N_4 \tag{5.7}$$

In a good laser system the relaxation rate from level 4 to level 3 must be very fast. Since level 3 has long lifetime $\tau_3 >> \tau_{4\to3}$. Therefore $N_3 >> N_4$. The equation (5.4) can be rewritten in the steady state as;

$$N_2 = \left(\frac{\tau_{2\to1}}{\tau_{3\to2}} + \frac{\tau_{4\to3}\tau_{2\to1}}{\tau_{4\to2}\tau_3} \right) N_3 = \beta N_3 \tag{5.8}$$

The parameter β depends on relaxation time rates only. If β is less than unity, there will be the desired population inversion from level 3 to level 2. In a good laser system $\gamma_{4\to2} \approx 0$ condition is revealed. In this case $\beta \approx \frac{\tau_{2\to1}}{\tau_{3\to2}}$. Then the condition for population inversion becomes

$$\beta = \frac{N_2}{N_3} \approx \frac{\tau_{2\to1}}{\tau_{3\to2}} << 1 \tag{5.9}$$

Another parameter for evaluating laser material is *fluorescent quantum efficiency* κ. κ is a dimensionless parameter defined as the number of fluorescent photons spontaneously emitted on the laser transition divided by the number of pump photons absorbed on the pump transition when the laser material is below threshold [51]. The quantum efficiency for a four level system is given by;

$$\kappa = \frac{\gamma_{4\to3}}{\gamma_4} \times \frac{\gamma_{rad}}{\gamma_3} = \frac{\gamma_4}{\gamma_{4\to3}} \times \frac{\gamma_3}{\gamma_{rad}} \tag{5.10}$$

γ_{rad} defined as the radiative decay rate from level 3 to level 2 ($\gamma_{rad} \equiv \gamma_{rad}(3 \to 2)$). The first ratio shows us the fraction of the total atoms that are pumped to level 4 and relax down directly to level 3 rather than relaxing down to another level incontrast the second ratio tells us the fraction of the total radiative decay from level 3 to level 2.

Considering steady state and fluorescent quantum efficiency conditions, we can obtain population inversion between level 3 and level 2 versus pumping strength for four level case as;

$$\frac{N_3 - N_2}{N} = \frac{(1-\beta)\kappa W_p \tau_{rad}}{1 + \left[(1+\beta) + 2\tau_{4\to 3}/\tau_{rad}\right]\kappa W_p \tau_{rad}} \tag{5.11}$$

In a good laser material case, the equation (5.11) can be written as;

$$\frac{N_3 - N_2}{N} \approx \frac{(1-\beta)\kappa W_p \tau_{rad}}{1 + \left[(1+\beta)\right]\kappa W_p \tau_{rad}} \approx \frac{W_p \tau_{rad}}{1 + W_p \tau_{rad}} \text{ if } \beta \to 0 \tag{5.12}$$

where N shows the total population in all levels at the steady state.

The threshold pump power for four level system is given [52]

$$P_{th} = \left(\frac{\alpha}{\eta_p}\right)\left(\frac{h\nu_p}{\tau_3}\right)\left[\frac{\pi(w_0^2 + w_p^2)}{2\sigma_{se}}\right] \tag{5.13}$$

Here P_{th} is the power required to reach threshold, α is the loss of the cavity, η_p is the pump efficiency, w_p is the pump spot size, w_0 is the spot size at beam waist and σ_{se} is the stimulated emission cross section.

The threshold pump intensity can be calculated by dividing equation (5.13) by area

$$I_{th} = \frac{P_{th}}{A} = \frac{\left(\frac{\alpha}{\eta_p}\right)\left(\frac{h\nu_p}{\tau_3}\right)\left[\frac{\pi(w_0^2 + w_p^2)}{2\sigma_{se}}\right]}{4\pi r^2} \tag{5.14}$$

Using (5.14) one can calculate threshold pump energy by multiplying pump period

$$E_{th} = I_{th} \times t \tag{5.15}$$

In our experiments, 100 ns pulsed Nd:YAG second harmonic green laser is used for excitation source. The threshold pump energy can be obtained as;

$$E_{th} = \frac{(\frac{\alpha}{\eta_p})(\frac{h\nu_p}{\tau_3})\left[\frac{\pi(w_0^2 + w_p^2)}{2\sigma_{se}}\right]}{4\pi r^2} \times 10^{-7} \text{ sec} \qquad (5.16)$$

5.4 Threshold Region

The lasing threshold is defined as the minimum power level at which laser oscillation starts. To analyze laser threshold behavior, we assume a low-loss cavity mode with photon number $n(t)$ and two level system which has upper level $N_2(t)$. We assume that the upper level is pumped with a constant rate of R_p atoms/seconds. The population decay from the upper level is given as γ_2. Lower laser level is assumed to decay fast so that $N_1 \approx 0$

The rate equation for the system is given as [51];

$$\frac{dn}{dt} = K(n+1)N_2 - \gamma_c n \text{ and } \frac{dN_2}{dt} = R_p - KnN_2 - \gamma_2 N_2 \qquad (5.17)$$

where γ_c is the cavity decay rate, K is the coupling constant $K = 3^* \gamma_{rad} / p$. p in this equation shows the cavity mode number and 3^* is the polarization number.

For the steady state solution where $d/dt = 0$, we can obtain below-threshold behavior for the first term of (5.17) as;

$$n_{ss} = \frac{N_{ss}}{\gamma_c / K - N_{ss}} = \frac{N_{ss}}{N_{th} - N_{ss}} \qquad (5.18)$$

where subscript ss designates the steady state behavior. The steady state solution of the second term becomes

$$N_{ss} = \frac{R_p}{\gamma_2 + Kn_{ss}} = R_p \tau_2 \times \frac{1}{1 + (\gamma_{rad} / \gamma_2) \times (n_{ss} / p)} \tag{5.19}$$

Equation 5.18 tells us that n_{ss}, the number of photons at steady state, will remain zero or very small until upper level population at steady state N_{ss} is raised by the fraction of a threshold inversion value N_{th} which is obtained as;

$$N_{th} = \frac{\gamma_c}{K} = \frac{\gamma_c}{\gamma_{rad}} p \tag{5.20}$$

5.5 Lasing from Single Water Microdroplet Standing on a Superhydrophobic Surface

Water microdroplets were excited with a frequency-doubled, Q-switched Nd:YAG laser which produced green pulses at the wavelength of 532 nm. The pulse repetition rate and pulsewidth were 1 kHz and 100 ns, respectively. In the experiments, pump energies up to 40 μJ/pulse were available. Excitation was achieved by focusing the pump beam to a 14 μm diameter spot. A high numerical aperture microscope objective (60x, NA=1.4) was used in the inverted geometry both for excitation and collection of the fluorescence. The collected fluorescence was transmitted through a dichroic mirror, a 1.5x magnifier element, and was dispersed by a ½-meter monochromator. The spectra were then recorded with a silicon CCD camera. With the selected 300 grooves/mm grating and input slit width of 30 μm, a spectral resolution of 0.24 nm was achieved. A shutter was used to block the pump

beam at all times except during the 50 ms exposure periods of the CCD camera. Pump power was adjusted using a variable-density filter [48].

Figures 5.3a-5.3c show the power dependent fluorescence spectra obtained from a 7.8 μm diameter microdroplet exhibiting laser emission. In Fig. 5.3a the intensity of the whispering gallery mode (WGM) at around 601 nm is comparable to the intensity of other WGMs and the background Rhodamine B emission. As shown in Figs. 5.3b and 5.3c, this WGM dominates the emission spectrum at higher excitation powers. The observed nonlinear power dependence is an indication of laser emission. The lasing WGM is spectrally located in the red-shifted portion of the Rhodamine B emission spectrum, near the gain maximum [48]. This is consistent with the previous demonstrations using microdroplets flying in air [47]. Due to the errors caused by the deviations from the ideal spherical geometry of the stationary microdroplets, no attempt was made to exactly identify the WGMs seen in Fig. 5.3. It is speculated that the lasing WGM has a mode order of 1 because of its high quality factor. Laser emission was observed to decay with photobleaching. Fig. 5.3d shows the 30th emission spectrum recorded after the spectrum shown in Fig. 5.3c, under a constant excitation fluence of $4950\,J/cm^2$. As can be seen in Fig. 5.3d, the intensity of the WGM at around 601 nm becomes comparable to the intensities of the other WGMs as a result of photobleaching, and lasing is no longer observed in this case [48].

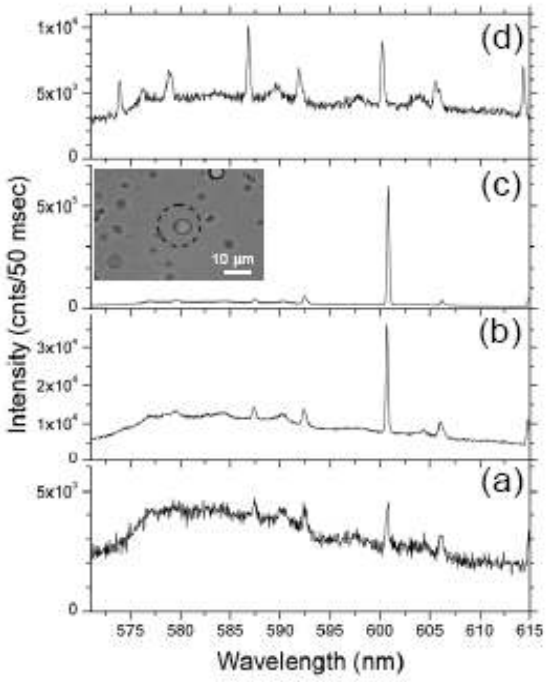

Figure 5. 3 (a-c) Power dependent emission spectra obtained from a 7.8 μm diameter glycerol/water microdroplet. Excitation fluences are 200 J/cm^2, 940 J/cm^2, and 4950 J/cm^2 in (a), (b), and (c) respectively. Inset: Optical microscope image of the microdroplet, dashed circle shows the area illuminated by the excitation laser. (d) 30th emission spectra obtained after the spectra shown in (c) under a constant excitation fluence of 4950 J/cm^2.

Power dependent intensities of the lasing WGM as well as two other WGMs and the background emission at 580 nm are plotted in Fig. 5.4. The emission from the WGMs at 587 nm and 592 nm, and the background emission at 580 nm show linear power dependences at low excitation powers. Above an excitation fluence of 1290 J/cm^2, they become saturated, without any clear indication of nonlinear power dependence. On the other hand, the lasing WGM exhibits nonlinear power dependence above certain threshold

excitation fluence. The threshold fluence was estimated from the crossing point of the linear least squares fits to the power-dependent emission data and was determined to be $750\,J/cm^2$. At high excitation powers, saturation was observed [48].

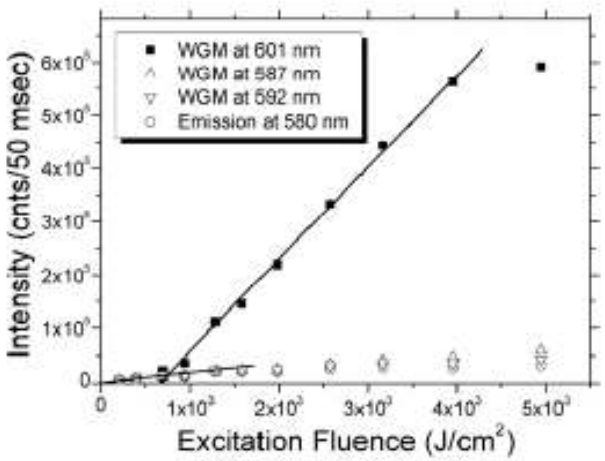

Figure 5. 4 Emission intensity vs. excitation fluence of a 7.8 μm diameter glycerol/water microdroplet for the lasing WGM (601 nm), two other WGMs (587 and 592 nm), and background emission at 580 nm.

Another indication of laser emission is the decrease in the spectral width of the lasing mode. This was observed for the specific lasing WGM shown in Figs. 5.5.a and 5.5.b. The fullwidth- at-half-maximum (FWHM) of the lasing WGM is measured to decrease from 0.34 nm at the excitation fluence of 200 J/cm^2 to a resolution-limited width of 0.25 nm at excitation powers exceeding $1290\,J/cm^2$. In Figure 5.5.a, we plot the dependence of the FWHM of another lasing WGM on the excitation fluence from a microdroplet with a diameter of 6.9 μm. In particular, the FWHM of this WGM is 0.54 nm at the relatively low excitation fluence of $990\,J/cm^2$. With the onset of lasing, the FWHM decreases down to 0.28 nm at the excitation fluence of $14840\,J/cm^2$ [48].

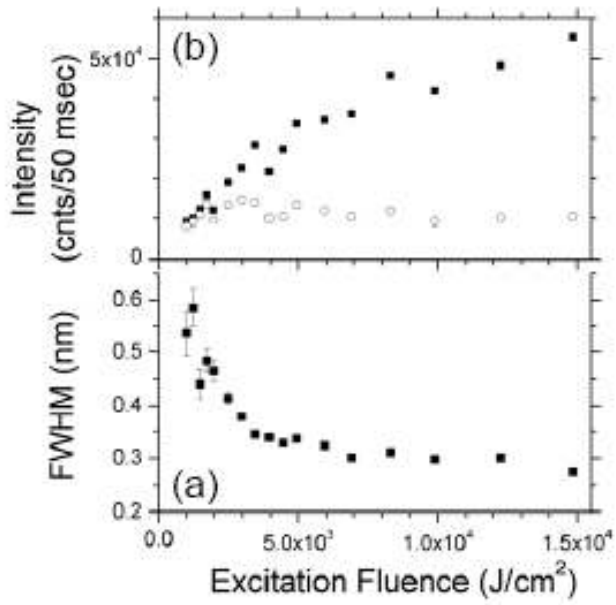

Figure 5. 5 (a) FWHM vs. excitation fluence for the lasing WGM of a 6.9 μm diameter glycerol/water microdroplet. (b) Emission intensity vs. excitation fluence for the lasing WGM (filled squares), and background emission at 580 nm (empty circles).

We have also observed instances where multimode lasing occurred. This is shown in Figure 5.6 where two WGMs oscillating at the wavelengths of 599 nm and 697 nm were seen to lase simultaneously in an 8.2 μm diameter microdroplet. As discussed above, uncertainties due to deviations from the ideal spherical geometry prevent the exact identification of the lasing WGMs. However, free spectral range (FSR) measurements suggest that they belong to two different sets of WGMs having different mode orders or polarizations. The two sets of WGMs are indicated by the letters A and B in the figure. The measured FSR for the sets A and B are 12.15 nm and 12.68 nm, respectively. WGMs in the set A have high quality factors relative to all other WGMs. This suggests that these WGMs

can have a mode order of 1 ($TE_{m,1}$ or $TM_{m,1}$). Estimations based on an ideal spherical microcavity suggest that the WGMs in set B have a mode order of 2 rather than 1. This makes physical sense because the spatial overlap between $TE_{m,1}$ and $TM_{m,1}$ WGMs increases the gain competition and decreases the possibility of simultaneous lasing. In contrast, there is sufficient mismatch between the spatial field distributions of the WGMs with mode orders 1 and 2, that both can lase simultaneously [48].

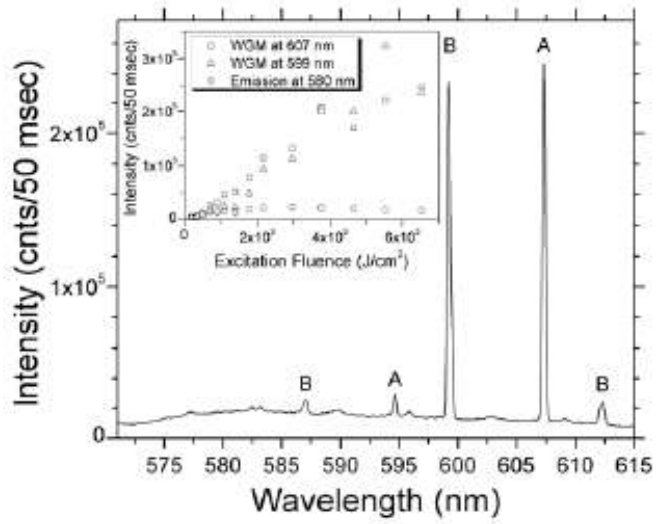

Figure 5. 6 Emission spectrum obtained from 8.2 μm diameter glycerol/water microdroplet exhibiting lasing at two WGMs at 599 and 607 nm. Excitation fluence is 6530 J/cm^2. Inset: Emission intensity vs. excitation fluence of the lasing WGMs, and background emission at 580 nm.

5.6 Summary

In this chapter, we demonstrated laser emission from single, stationary, Rhodamine B-doped glycerol/water microdroplets located on a superhydrophobic surface. In the experiments, a pulsed, frequency-doubled Nd:YAG laser operating at 532 nm was used as the excitation source. The microdroplets ranged in diameter from a few to 20 μm. Lasing was achieved in the red-shifted portion of the dye emission spectrum with threshold fluences as low as 750 J/cm^2. Photobleaching was observed when the microdroplets were pumped above threshold. In certain cases, multimode lasing was also observed and attributed to the simultaneous lasing of two modes belonging to different sets of whispering gallery modes [48].

As optical microcavities exhibiting laser emission, microdroplets standing on a superhydrophobic surface can be attractive alternatives to solid optical microcavities standing on substrates, e.g. microdisks, micropillars, photonic crystal defect microcavities. Microdroplets standing on a superhydrophobic surface do not pose any microfabrication challenges. They also bring together the advantage of easy deformability. This can lead to the realizations of tunable microcavity lasers by using evaporation/condensation, or electric field tuning. In addition, lasing stationary microdroplets can be potentially used as an optical diagnostic tool in high-resolution surface characterization.

Chapter 6

RAMAN LASING FROM STATIONARY GLYCEROL/WATER MICRODROPLETS STANDING ON A SUPERHYDROPHOBIC SURFACE

6.1 Introduction

Optical microcavities enable low-threshold stimulation Raman lasing because of their small mode volumes and high quality factors. Extensive studies have been performed to investigate resonant Raman scattering in liquid microdroplet streams[53], electrodynamically levitated microparticles[54], or optically trapped liquid microdroplets[55]. However, to date, only cavity enhanced Raman scattering (CERS) has been reported with microdroplets. In addition, resonant Raman emission characteristics of stationary microdroplets located on a surface have not been reported. In this chapter, we investigate Raman lasing from stationary microdroplets situated on a superhydrophobic surface. In the experiments, we identified two distinct regimes of operation by using glycerol-water microdroplets on a superhydrophobic surface coated with silica nanoparticles: cavity-enhanced Raman scattering and Raman lasing [56].

6.2 Raman Scattering

Raman scattering is an inelastic scattering process, which was first observed by Indian physicist Chandrasekhara Venkata Raman in 1922 [57]. The scattering is caused by the temporal modulation of molecular polarizability of the medium. Each molecule's polarization response is periodically modulated by intermolecular kinetics, vibration or rotation [58]. As a result of this modulation, the frequency of scattered light may be lower or higher than the frequency of incident light. The shift in the scattered frequency is caused by either Stokes scattering or Anti-Stokes scattering (Figure 6.1) . In Stokes scattering, there will be a transition from ground state g to a virtual level associated with the excited state n' with the frequency v. This transition is fallowed by downward transition from the virtual level to a final state n with a frequency v_s. Because of the frequency change, red-shifting of the scattering photon is observed and a phonon is created. On the other hand, in the Anti-Stokes scattering, the transition occurs from the intermediate level to virtual level. This transition is reversed by downward transition from the virtual level to ground state with a frequency v_{as}. Since the scattered photon has a higher frequency, blue-shifting can be detected in the scattering light and the absorption of a phonon is observed [59]. The intensity of the Stokes scattering is orders of magnitude more intense than the Anti-Stokes because in thermal equilibrium the population of the final level is smaller than the population of the initial level by the factor of $\exp(-\hbar v / k_B T)$. For the majority of Raman scattering studies, the frequency shift is in the range of 10^2-10^3 cm^{-1} because of the high molecular vibrational motion.

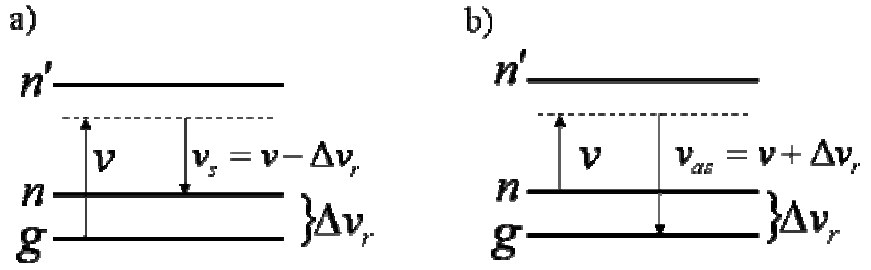

Figure 6. 1 Energy level diagrams describing a) Stokes shifted, b) Anti stokes shifted Raman Scattering

6.3 Stimulated Raman Scattering in Microcavities

The lasing threshold occurs when the cavity round-trip gain equals round trip loss. The threshold pump power to achieve Stimulated Raman Scattering is derived as[60]

$$P_{th} = \frac{\pi^2 n^2 V_{eff}}{\lambda_p \lambda_R C(\Gamma) g_R^B} Q_e^P \left(\frac{1}{Q_T^P}\right)^2 \frac{1}{Q_T^R} \tag{6.1}$$

Here λ_p and λ_R are the wavelength of the pump and Raman respectively. V_{eff} is the effective pump mode volume and given as $V_{eff} = \frac{\int |E_p|^2 dv \int |E_R|^2 dv}{\int |E_p|^2 |E_R|^2 dv}$ where E_p is the amplitude of the intra-cavity pump and E_R is the amplitude of Raman. g_R^B is the nonlinear bulk Raman gain coefficient (in units of m/W). $C(\Gamma)$ is a circulating power correction factor. Q_T^p is the total quality factor for the pump mode, with the contribution of intrinsic mode quality factor Q_0^p and coupling mode quality factor Q_e^p. The equation 6.1 shows that

high Q microcavities reduce the pump power required for stimulated Raman scattering. Furthermore the threshold power is proportional to the factor V/Q^2 which is the multiplication of the Purcell Factor [61] ($\propto Q/V$) by quality factor. The total Raman output power is given by [62];

$$P_R = 4\frac{w_R}{w_P}(1+\frac{\tau_{ex}}{\tau_0})^{-2}P_{th}\left(\sqrt{\frac{P}{P_{th}}}-1\right) \tag{6.2}$$

where w_R and w_P are the excitation frequency of Raman and pump modes respectively. τ_0 and τ_{ex} are the intrinsic and external photon lifetimes. P is the pump power .

6.4 Observation of Cavity Enhanced Raman Scattering (CERS)

With smaller microdoplets, generated using the ultrasonic nebulizer, we were able to observe cavity-enhanced Raman scattering (CERS). Figure 6.2 shows the CERS spectrum of a 10.9-μm-diameter microdroplet, recorded using a total exposure time of 45 sec. In this spectrum, the whispering gallery modes (WGMs) are clearly visible together with the Raman emission bands of the glycerol-water solution. In Fig. 6.2, free spectral ranges (FSRs) of 10.6 nm and 10.8 nm are measured for the WGMs indicated by A and B respectively. For a 10.9-μm-diameter ideal glycerol microsphere, an FSR of 8.9 nm is expected. The deviation of the observed FSRs from 8.9 nm indicates the nonsphericity in the geometry of the microdroplet standing on a superhydrophobic surface[10]. Despite the high excitation power, none of the WGMs dominated the spectrum and hence no clear evidence for Raman lasing was observed. The absence of lasing is mainly attributed to low Q factors of the WGMs of smaller microdroplets. Full width at half maximum (FWHM) of the WGMs revealed Q factors of up to ~2000 in this case [56].

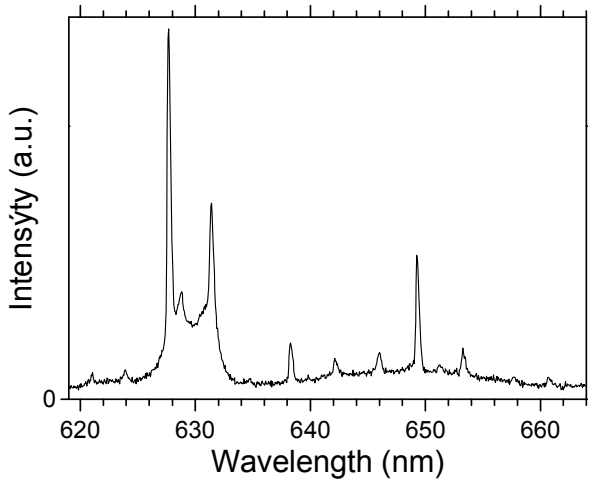

Figure 6. 2 Cavity-enhanced Raman scattering spectrum of a 10.9-μm-diameter glycerol-water microdroplet. Exposure time is 45 sec.

6.5 Observation of Raman Lasing from Glycerol/Water Microdroplets

Raman lasing was routinely observed in larger microdroplets generated with the atomizer. As an example, Fig. 6.3 shows the spectra obtained from a 12.4-μm-diameter microdroplet, showing Raman lasing. During a series of consecutive acquisitions, intense WGM emission is momentarily observed in the high gain region of the Raman bands at 632.3 nm, as shown in Fig. 6.3(a). This is a clear indication of Raman lasing. Raman lasing is not sustained, and the intensity of the lasing WGM drops by more than 30 dB in the consecutive acquisition (Fig. 6.3(b)). The inset in Fig. 6.3(a) shows the "on/off" behavior observed during 20 acquisitions for this microdroplet. At acquisitions 7, 9, and 13, high intensity Raman lasing is observed, while the collected intensity is much smaller during the

remaining acquisitions. Despite the "on/off" behavior, the spectral location of the lasing WGM remains stable, indicating a constant droplet size within the spectral resolution of the measurement setup [56].

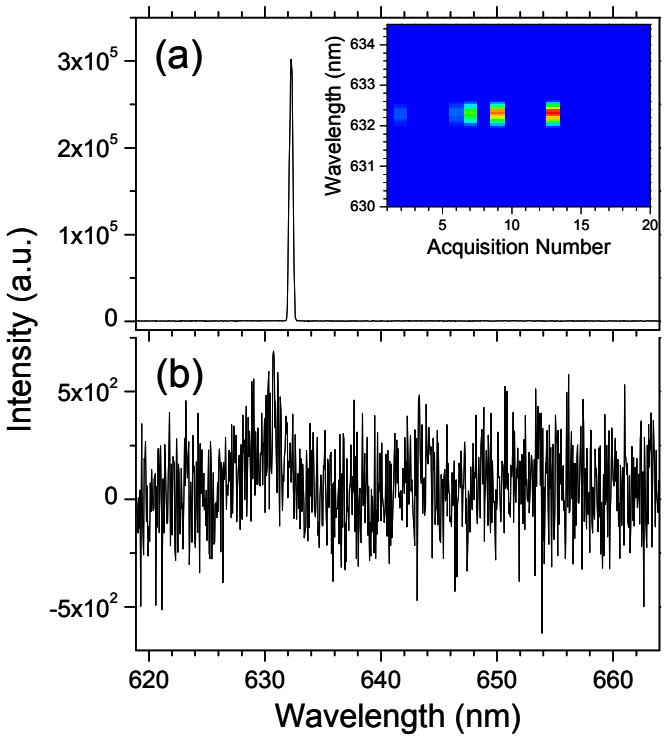

Figure 6. 3(a) Measured spectrum obtained from a 12.4-μm-diameter microdroplet, showing Raman lasing. (b) Corresponding spectrum during the non-lasing period. Inset shows the consecutive spectra (exposure time: 1sec) showing the "on-off" behavior. Intensity values in arbitrary units increase from blue to red.

In order to investigate the origin of Raman lasing, we recorded the Raman spectra of glycerol-water mixtures of various compositions. Figure 6.4 shows the acquired spectra

for solutions containing 100 (Curve A), and 13 (Curve B) vol. % water. As can be seen, the band centered around 630 nm originates from glycerol and dominates in the mixture containing 13 vol. % water. Even in a mixture containing 50 vol. % water, the peak of the glycerol band near 630 nm was larger than that of the 650 nm band by more than 60 %. After reaching the equilibrium sizes, the investigated microdroplets have a Raman spectrum similar to that in Fig. 6.4(d). Hence, this indicates that Raman lasing occurs due to the presence of glycerol which has a larger Raman gain than that of water in the 620-660 nm spectral window (see Fig. 6.4) [56].

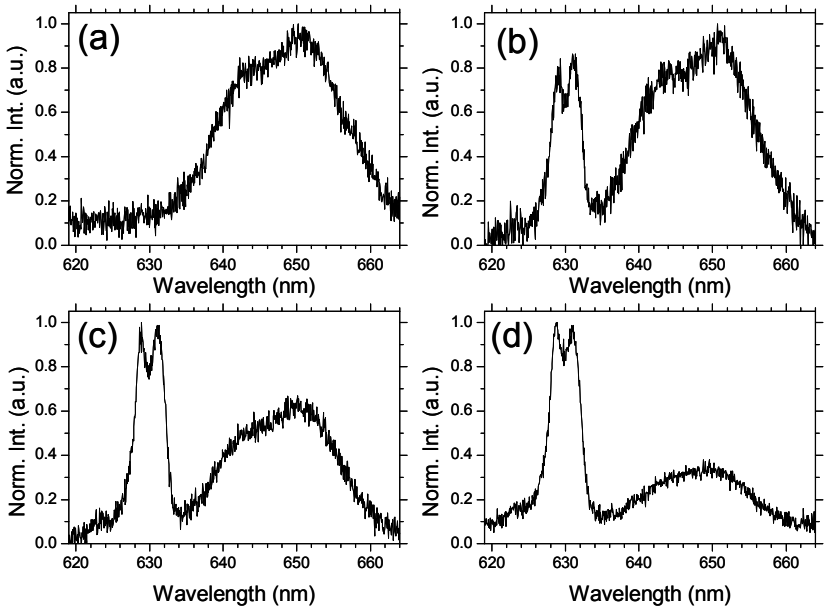

Figure 6. 4 Normalized Raman spectra of glycerol-water mixtures containing (a) 100, (b) 75, (c) 50, and (d) 13 vol. % water. Exposure time is 30 sec.

Without an exception, “on/off” behavior was observed in all microdroplets showing Raman lasing. This phenomenon is attributed to density fluctuations caused by local heating of the microdroplets during lasing. As a result, the circulating mode acquires a spatially distorted phase and can no longer satisfy the resonance condition. During the “off” period, excess generated heat is sinked, and Raman lasing resumes once the microdroplet cools down. The experiments performed by applying a flow of dry nitrogen onto the microdroplet revealed significant decrease in the inter-burst time separations, indicating the major role played by the convective cooling mechanism. In Fig. 6.5, we plot the time trace of the Raman lasing intensity observed from a 21.5-μm-diameter microdroplet. This time trace was generated by analyzing the video of the Raman signal collected from the microdroplet (recorded at a rate of 25 frames/sec). At each frame, intensity was calculated by integrating the brightness over a box including the microdroplet. The box used in calculating the time trace is shown in Fig. 6.5 at three different frames. The ring pattern of the lasing mode is visible in frames 3348 and 12083, while very low intensity is collected in frame 3349, corresponding to an “off” period. Nitrogen purging was applied to this microdroplet only between frames 3000-6000 and 9000-12000. During these time intervals, average inter-burst separation was observed to decrease from 58.6 frames (2.3 sec) to 10.2 frames (0.4 sec) because of the increased convective cooling efficiency. A detailed analysis of the “on/off” behavior which takes into account conductive as well as convective cooling is currently underway in our laboratory. We think that the cooling mechanism and the superhydrophobic surface can be further optimized in order to decrease the inter-burst separations [56].

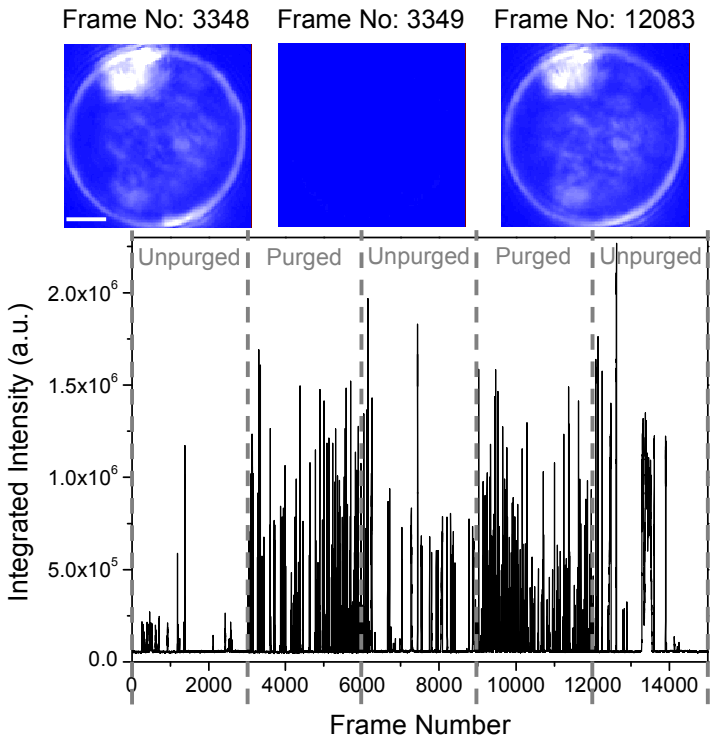

Figure 6. 5 Recorded time trace of the Raman lasing intensity observed from a 21.5-μm-diameter microdroplet. Nitrogen purging is on between frames 3000-6000, and 9000-12000. Average inter-burst separations are 2.3 sec and 0.4 sec during the unpurged and purged periods respectively. Images used in calculating the time trace at frames 3348, 3349, and 12083 are shown at the top. Coloration in the images shows the grayscale intensity increasing from blue to white. Scale bar shows 5 μm.

6.6 Summary

In this chapter, we have demonstrated CERS and Raman lasing from stationary, glycerol-water microdroplets situated on a superhydrophobic surface coated with silica nanoparticles. In the experiments, microdroplets with radii in the 11-15 μm range were pumped at 532 nm by using a pulsed, frequency-doubled Nd:YAG laser. Measurements gave clear indication of Raman lasing within the Raman band of glycerol, not previously observed in other studies with microdroplets. The contrast ratio of the Raman laser signal was larger than 30 dB. Furthermore, neither geometrical deformation nor spatial relocation of the microdroplet was observed during the detection periods that extended up to tens of minutes. Raman lasing was, however, not sustained and occurred in temporally separated bursts. Detailed investigation with microdroplets of various sizes indicates that the average time between lasing bursts is of the order of 2-2.5 sec. We note that the novel configuration based on the superhydrophobic surface obviates the need for additional trapping schemes such as electrodynamic levitation and optical trapping[63, 64]. Finally, the system described here could pave the way to the development of very compact, cost-effective light sources for short-haul communications systems by using readily available pump sources such as the 532-nm, second harmonic of the Nd:YAG laser.

Chapter 7

CONCLUSIONS

Optical microcavities confine light into small volumes in high quality resonances. Up to date various geometries have been demonstrated to function as optical microcavities. Cylindrical, spherical, spheroidal/toroidal, ring, and other shapes and topologies with various confining principles have been used in these demonstrations. Optical microcavities have so far found various applications in both fundamental and applied research areas such as cavity quantum electrodynamics, optoelectronics, and biological sensing. In this thesis, we introduced a novel optical microcavity: a glycerol/water microdroplet standing on a superhydrophobic surface. By using a home-built current controlled humidity chamber, large spectral tunability of WGMs from Rhodamine B dye doped single water microdroplet is observed by changing condensation and evaporation kinetics of the droplets. Since size control is an important challenge in applications of microdroplets and liquids, we demonstrated a self control mechanism stabilizing water microdroplets by laser absorption phenomena. The mechanism relies on the interplay between the condensation rate that was kept constant and evaporation rate induced by laser excitation which critically depends on the size of the microdroplets. Water microdroplets stayed in the same size during long time periods. We investigated also laser emission from Rhodamine B doped glycerol/water microdroplets. A second harmonic generation pulsed laser is applied to excite laser emission in the red-shifted portion of the dye emission spectrum. Single lasing mode is observed in 601 nm whereas multimodes lasing is observed at 599 nm and 607 nm. Under

the excitation of high laser power, glycerol/water microdroplets exhibited cavity enhanced Raman scattering and Raman lasing. Cavity enhanced Raman scattering is observed in smaller diameter microdroplets, up to 11 μm, because of their low Q factors. On the other hand, large diameter droplets, up to 21 μm, are exhibited Raman lasing near 632 nm with random bursts, two-burst separation is about 2-2.5 sec. The random burst is due to local heating of the droplet. After a lasing, it starts to cool its down and lase again. When dry nitrogen is purged on it to cool externally, time period of burst separation is reduced to 0.4 sec.

APPENDIX A

Matlab Programming of Modified Absorption Efficiency ($\widetilde{Q}_{abs}$)

Calculation Of Peaks In Alpha Interval

```
clear all;
alpha_min = 30;
alpha_max = 50;

res_n=1.33+i*40*10^-6;
lambda = 532*10^-9;

dx=0.001;
x=dx:dx:alpha_max;
res_radius=x*lambda/(2*pi);

lmax = 5 + round(max(x) + 4.3*max(x)^(1/3) + 2);

unique_index = 1;
for l=1:lmax;
   j=sqrt(pi./(2*x)).*besselj(l+1/2,x);
   j_bar=sqrt(pi./(2*res_n*x)).*besselj(l+1/2,res_n*x);
   % spherical bessel function

   h1=sqrt(pi./(2*x)).*besselh(l+1/2,1,x);
   % spherical hankel function

   d_x_j=diff(x.*j)/(dx);
   d_x_j(length(d_x_j)+1)=d_x_j(length(d_x_j));

   d_x_h1=diff(x.*h1)/(dx);
   d_x_h1(length(d_x_h1)+1)=d_x_h1(length(d_x_h1));
```

```
   d_x_j_bar=diff(res_n*x.*j_bar)/(res_n*dx);
   d_x_j_bar(length(d_x_j_bar)+1)=d_x_j_bar(length(d_x_j_bar));

   a_l=((res_n^2)*j_bar.*d_x_j-j.*d_x_j_bar)./...
      ((res_n^2)*j_bar.*d_x_h1-h1.*d_x_j_bar);
   b_l=(j_bar.*d_x_j-j.*d_x_j_bar)./...
      (j_bar.*d_x_h1-h1.*d_x_j_bar);


   %d1 = 2 + find( (a_l(3:length(a_l)-2)>a_l(2:length(a_l)-3)) & (a_l(3:length(a_l)-
2)>a_l(4:length(a_l)-1)));
   [d0,d1]=localmax(a_l,10);
   d2 = find(x(d1)>=alpha_min);
   for d3 = 1:length(d2)
   label(unique_index,:) = cat(2,'TE MODE, NO: ',cat(2,blanks(10-
length(num2str(l))),num2str(l)),', ORDER: ',cat(2,blanks(10-
length(num2str(d2(d3)))),num2str(d2(d3))));
   location(unique_index,1) = unique_index; location(unique_index,2) = x(d1(d2(d3)));
   unique_index = unique_index + 1;
   end

   %d1 = 2 + find( (b_l(3:length(b_l)-2)>b_l(2:length(b_l)-3)) & (b_l(3:length(b_l)-
2)>b_l(4:length(b_l)-1)));
   [d0,d1]=localmax(b_l,10);
   d2 = find(x(d1)>=alpha_min);
   for d3 = 1:length(d2)
   label(unique_index,:) = cat(2,'TM MODE, NO: ',cat(2,blanks(10-
length(num2str(l))),num2str(l)),', ORDER: ',cat(2,blanks(10-
length(num2str(d2(d3)))),num2str(d2(d3))));
   location(unique_index,1) = unique_index; location(unique_index,2) = x(d1(d2(d3)));
   unique_index = unique_index + 1;
   end

   disp(l)
end

location = sortrows(location,2);
disp(cat(2,'The interval includes a total of ',num2str(length(location)),' modes. These are: '))
```

```
for d4 = 1:length(location)
   disp(cat(2,label(location(d4,1),:),'  LOCATION: ',num2str(location(d4,2)),'  R:
',num2str(location(d4,2)*532/2/pi)))
end
```

Finding Convolved ($\widetilde{Q}_{abs}$)

```
function Qabstilda = convolvedQabstilda(Pabs,Pbeam)
% Pabs and Pbeam are Nx2 arrays for absorbed and incident powers respectively.
% First column: alpha values (should be in ascending order), Second column:
% corresponding power. Use sortrows(***,1) before calling
% convolvedQabstilda if alpha values are not in order.

lambda0 = 532; %nm's
lambda_range = 2; % i.e. if lambda_range = 2, the minimum wavelength emmitted from
the
                % laser is 532-1=531, and the maximum is 532+1=533
gamma = 0.1; %Full width at half maximum (in nm's)
discpre = 200; %Discritization precision
lambda = [lambda0-lambda_range/2:lambda_range/discpre:lambda0+lambda_range/2];
I = (gamma^2/4)./((lambda-lambda0).^2 + gamma^2/4);
I = cat(2,lambda',I');  % I is the laser profile. First column: wavelength
                    % Second column: Intensity that corresponds (1 at lambda_zero)

% In the for loop below, we define 3D arrays for absorbed and incident
% powers. Third dimension is to cover the wavelength range emitted from the laser.
% Meanwhile alphas are converted into R (radius) by R=alpha*lambda/2pi,
% and powers are weighted according to second column of I.
for i = 1:length(I)
   Pabs2(:,1,i) = Pabs(:,1)*I(i,1)/(2*pi);
   Pabs2(:,2,i) = Pabs(:,2)*I(i,2);

   Pbeam2(:,1,i) = Pbeam(:,1)*I(i,1)/(2*pi);
   Pbeam2(:,2,i) = Pbeam(:,2)*I(i,2);
end

Rmin = max(Pabs2(1,1,:));  Rmax = min(Pabs2(length(Pabs),1,:));
% could use Pbeam2 and Pbeam as well. Rmin and Rmax are the min and max
```

```
% values of x-axis of the resulting Qabs vs. R graph.

R = [Rmin:(Rmax-Rmin)/(length(Pabs)-2):Rmax];

% We use interpolation to find the powers that correspond to the radius values
% in the R array. We do this for each "frame" of the Pabs2 and Pbeam2. New
% R vs. Power arrays are stored in Pabs3 and Pbeam3 that have the same
% structure as Pabs2 and Pbeam2.
for i = 1:length(I)
   Pabs3(:,1,i) = R;
   Pabs3(:,2,i) = interp1(Pabs2(:,1,i),Pabs2(:,2,i),R);

   Pbeam3(:,1,i) = R;
   Pbeam3(:,2,i) = interp1(Pbeam2(:,1,i),Pbeam2(:,2,i),R);
end

% Sum the absorbed and incident powers over the whole spectrum of wavelengths
% to obtain their total values.
Pabstotal = (lambda_range/discpre)*sum(Pabs3(:,2,:),3); Pbeamtotal =
(lambda_range/discpre)*sum(Pbeam3(:,2,:),3);

Qabstilda(:,1) = R; Qabstilda(:,2) = Pabstotal./Pbeamtotal;

figure1 = figure;
axes1 = axes(...
'FontSize',14,...
'XGrid','on',...
'YGrid','on',...
'Parent',figure1);
title(axes1,cat(2,'\lambda = ',num2str(lambda0),'\pm',num2str(lambda_range/2),'nm',',
\Gamma = ',num2str(gamma),'nm'));
xlabel(axes1,'R');
xlim([Rmin Rmax])
ylabel(axes1,'P_a_b_s/P_i_n_c');
hold(axes1,'all');

plot1 = plot(Qabstilda(:,1),Qabstilda(:,2),'Marker','*');

figure; plot(I(:,1),I(:,2),'-*'); xlabel('\lambda'); ylabel('I'); title('Laser Profile');
```

Calculation of Local Max

```
function [lmval,indd]=localmax(xx,filt)
%LMAX        [lmval, indd]=lmax(xx,filt). Find local maxima in vector XX,where
%        LMVAL is the output vector with maxima values, INDD  is the
%        corresponding indexes, FILT is the number of passes of the small
%        running average filter in order to get rid of small peaks.  Default
%        value FILT =0 (no filtering). FILT in the range from 1 to 3 is
%        usially sufficient to remove most of a small peaks
%        For example:
%        xx=0:0.01:35; y=sin(xx) + cos(xx ./3);
%        plot(xx,y); grid; hold on;
%        [b,a]=lmax(y,2)
%         plot(xx(a),y(a),'r+')
%        see also LMIN, MAX, MIN

%************************************************|
%        Serge Koptenko, Guigne International Ltd., |
%        phone (709)895-3819, fax (709)895-3822     |
%--------------06/03/97----------------------------|

x=xx;
len_x = length(x);
          fltr=[1 1 1]/3;
  if nargin <2, filt=0;
          else
x1=x(1); x2=x(len_x);
          for jj=1:filt,
          c=conv(fltr,x);
          x=c(2:len_x+1);
          x(1)=x1;
       x(len_x)=x2;
          end
  end
lmval=[]; indd=[];
i=2;               % start at second data point in time series
    while i < len_x-1,
```

```
          if x(i) > x(i-1)
            if x(i) > x(i+1)          % definite max
lmval =[lmval x(i)];
indd = [ indd i];
            elseif x(i)==x(i+1)&x(i)==x(i+2)    % 'long' flat spot
%lmval =[lmval x(i)];            %1    comment these two lines for strict case
%indd = [ indd i];       %2 when only  definite max included
i = i + 2;                    % skip 2 points
            elseif x(i)==x(i+1)   % 'short' flat spot
%lmval =[lmval x(i)]; %1    comment these two lines for strict case
%indd = [ indd i];       %2 when only  definite max included
i = i + 1;                    % skip one point
            end
          end
          i = i + 1;
   end
if filt>0 & ~isempty(indd),
          if (indd(1)<= 3)|(indd(length(indd))+2>length(xx)),
            rng=1;          %check if index too close to the edge
          else rng=2;
          end
            for ii=1:length(indd),           % Find the real maximum value
              [val(ii) iind(ii)] = max(xx(indd(ii) -rng:indd(ii) +rng));
              iind(ii)=indd(ii) + iind(ii)  -rng-1;
            end
  indd=iind; lmval=val;
else
end
```

VITA

Mehmet Ali Dündar completed the high school in Hacı Ahmet Lisesi, Adana, Turkey, in 2000. He received his B. Sc. degree in physics from Koç University, Istanbul, Turkey, in 2005. He joined the M. Sc. program in Physics at Koç University in 2005. He received his M. Sc. degree from Koc University in 2007. His master thesis work was titled as "Introducing a Novel Optical Microcavity: A Glycerol/Water Microdroplet On a Superhydrophobic Surface." He will start his Ph. D degree at Technical University of Eindhoven in the Netherlands working on "Photonic Crystal Tunable Nanocavity". He is a student member of International Society for Optical Enginnering (SPIE) and Optical Society of America (OSA).

LIST OF PUBLICATIONS

1) A. Kiraz, A. Kurt, M. A. Dündar, and A. L. Demirel. “Simple largely tunable optical microcavity” Appl. Phys. Lett. 89, 081118 (2006)

2) A. Kiraz, A. Sennaroglu, S. Doğanay, M. A. Dündar, A. Kurt, H. Kalaycıoğlu, and A. L. Demirel. " Lasing from single, stationary, dye-doped glycerol/water microdroplets located on a superhydrophobic surface” Opt. Commun. 276, 145-148 (2007)

3) A. Kiraz, A. Kurt, M. A. Dündar, M. Y. Yüce, and A. L. Demirel. “Volume stabilization of single, dye-doped water microdroplets with femtoliter resolution” J. Opt. Soc. Am. B 24, 1824-1828 (2007)

4) A. Sennaroglu, A. Kiraz, M. A. Dündar, A. Kurt, and A. L. Demirel. “Raman lasing near 630 nm from stationary glycerol-water microdroplets on a superhyrophobic surface” to appear in Opt. Lett. (2007)

BIBLIOGRAPHY

[1] V. S. Ilchenko and A. B. Matsko, "Optical Resonators With Whispering-Gallery Modes—Part II: Applications," *IEEE JOURNAL OF SELECTED TOPICS IN QUANTUM ELECTRONICS*, vol. 12, pp. 15, 2006.

[2] C. J. Hood, H. J. Kimble, and J. Ye, "Characterization of high-finesse mirrors: Loss, phase shifts, and mode structure in an optical cavity," *Phys. Rev. A*, vol. 57, pp. 2293-2296, 2001.

[3] T. Baba, P. Fujita, A. Sakai, M. Kihara, and R. Watanabe, "Lasing characteristics of GaInAsP-InP strained quantum-well microdisk injection lasers with diameter of 2-10 /spl mu/m," *IEEE Photon. Tech. Lett.*, vol. 9, pp. 878-880, 1997.

[4] A. Belarouci, K. B. Hill, Y. Liu, Y. Xiong, T. Chang, and A. E. Craig, "Design and modeling of waveguide-coupled microring resonator," *Journal of Luminescence*, vol. 94-95, pp. 35-38, 2001.

[5] V. L. Seguin, "Whispering-gallery mode lasers with doped silica microspheres," *Optical Materials*, vol. 11, pp. 153-165, 1999.

[6] J. Scheuer and A. Yariv, "Annular Bragg Defect mode Resonators," *J. Opt. Soc. Am. B*, vol. 20, pp. 2285-2291, 2003.

[7] D. K. Armani, T. J. Kippenberg, S. M. Spillane, and K. J. Vahala, "Ultra-high-Q toroid microcavity on a chip," *Nature*, vol. 421, pp. 925-928, 2003.

[8] G. S. Solomon, M. Pelton, and Y. Yamamoto, "Single-mode Spontaneous Emission from a Single Quantum Dot in a Three-Dimensional Microcavity," *Phys. Rev. Lett.*, vol. 86, pp. 3903-3906, 2001.

[9] O. Painter, R. K. Lee, A. Scherer, A. Yariv, J. D. O'Brien, P. D. Dapkus, and I. Kim, "Two-dimensional photonic band-gap defect mode laser," *Science*, vol. 284, pp. 1819, 1999.

[10] A. Kiraz, A. Kurt, M. A. Dündar, and A. L. Demirel, "Simple largely tunable optical microcavity," *Appl. Phys. Lett.*, vol. 89, pp. 081118, 2006.

[11] K. J. Vahala, "Optical microcavities," *Nature*, vol. 424, pp. 839-846, 2003.

[12] V. Sandoghdar, F. Treussart, J. Hare, V. Lefevre-Seguin, J.-M. Raimond, and S. Haroche, "Very low threshold whispering-gallery-mode microsphere laser," *Phys. Rev. A*, vol. 54, pp. R1777, 1996.

[13] A. Ashkin and J. M. Dziedzic, "Observation of resonances in the radiation pressure on dielectric spheres," *Phys. Rev. Lett.*, vol. 38, pp. 1351-1354, 1977.

[14] A. Ashkin and J. M. Dziedzic, "Observation of optical resonances of dielectric spheres by light scattering," *Appl. Opt.*, vol. 20, pp. 1803, 1981.

[15] S. Arnold, S. Holler, and S. D. Druger, "Imaging enhanced energy transfer in a levitated aerosol particle," *J. Chem. Phys.*, vol. 104, pp. 7741-7748, 1996.

[16] W. K. C. G. B. Garrett, and W. L. Bond, "Stimulated emission into optical whispering gallery modes of spheres," *Phys. Rev.*, vol. 124, pp. 1807, 1961.

[17] M. Y. Yüce, A. L. Demirel, and F. Menzel, "Tuning the surface hydrophobicity of polymer/nanoparticle composite films in the wenzel regime by composition," *Langmuir*, vol. 21, pp. 5073-5078, 2005.

[18] C. Hsieh, J. M. Chen, R. R. Kuo, T. S. Lin, and C. F. Wu, "Influence of surface roughness on water- and oil-repellent surfaces coated with nanoparticles," *Applied Surface Science*, vol. 240, pp. 318, 2005.

[19] J. P. Barton, D. R. Alexander, and S. A. Schaub, "Internal fields of a spherical particle illuminated by a tightly focused laser beam: Focal point positioning effects at resonance," *J. Appl. Phys.*, vol. 65, pp. 2900-2906, 1989.

[20] J. P. Barton, D. R. Alexander, and S. A. Schaub, "Internal and near-surface electromagnetic fields for a spherical particle irradiated by a focused laser beam," *J. Appl. Phys.*, vol. 64, pp. 1632-1639, 1988.

[21] D. R. H. C.F Bohren, *Absorption and Scattering of Light by Small Particles*. New York: John Wiley&Sons, 1983.

[22] L. Rayleigh, "The problem of the whispering gallery," *Phil. Mag.*, vol. 20, pp. 1001-1004, 1910.

[23] J. T. K. and. M. K. W. K. P. Chylek, "Optical levitation and partial-wave resonances," *Phys. Rev. A*, vol. 18, pp. 2229-2233, 1978.

[24] P. Chylek, J. T. Kiehl, and M. K. W. Ko, "Optical levitation and partial-wave resonances," *Phys. Rev. A*, vol. 18, pp. 2229-2233, 1978.

[25] V. R. P. Chylek, A. Ashkin and J.m. Dziedzic, "Simultaneous determination of refractive indez and size of spherical dielectric particles from light scattering data," *Appl. Opt.*, vol. 22, pp. 2302, 1983.

[26] P. Urquhart, "Compound optical-fiber-based resonators," *J. Opt. Soc. Am. A*, vol. 5, pp. 803, 1988.

[27] H. C. Tapalian, J. P. Laine, and P. A. Lane, "Thermooptical switches using coated microsphere resonators," *IEEE Photon. Technol. Lett.*, vol. 14, pp. 6138, 2002.

[28] V. B. Braginsky, M. L. Gorodetsky, and V. S. Ilchenko, "Quality-Factor and Nonlinear Properties of Optical Whispering-Gallery Modes," *Physics Letters A*, vol. 137, pp. 393, 1989.

[29] V. S. Ilchenko and A. B. Matsko, "Optical Resonators with Whispering-Gallery Modes- Part:II: Applications," *IEEE Journal of Selected Topics in Quantum Electronics*, vol. 12, pp. 15, 2006.

[30] V. M. N. P. M.N Armenise, F. De Leonardis, and M. Armenise, "Modeling and design of a novel miniaturized integrated optical sensor for gyroscope systems," *J. Lightw. Technol.*, vol. 19, pp. 1476, 2001.

[31] J. M. G. B. Gayral, A. Lamaitre, C. Dupuis, L. Manin and J. Pelouard, "High-Q wet etched GaAs microdisks containing InAs quantum boxes," *Appl. Phys. Lett.*, vol. 75, pp. 1908, 1999.

[32] V. S. Ilchenko and A. B. Matsko, "Optical Resonators with Whispering-Gallery Modes- Part I: Basics," *IEEE Journal of Selected Topics in Quantum Electronics*, vol. 12, pp. 3, 2006.

[33] A. Ishumaru, *Wave Propagation and Scattering in Random Media*, vol. 1. Orlando, FL: Academic Press, 1978.

[34] R. E. Benner, P. W. Barber, J. F. Owen, and R. K. Chang, "Observation of Structure Resonances in the Fluorescence Spectra from Microspheres," *Phys. Rev. Lett.*, vol. 44, pp. 475-478, 1980.

[35] S.-X. Qian, J. B. Snow, H. M. Tzeng, and R. K. Chang, "Lasing Droplets: Highlighting the Liquid-Air Interface by Laser Emission," *Science*, vol. 231, pp. 486-488, 1986.

[36] A. Serpengüzel, J. C. Swindal, R. K. Chang, and W. P. Acker, "Two-dimensional imaging of sprays with fluorescence, lasing, and stimulated Raman scattering," *Appl. Opt.*, vol. 31, pp. 3543-3551, 1992.

[37] R. L. W. v. Klitzing, V. S. Ilchenko, J. Hare and V. L. Seguin, "Tunable whispering gallery modes for spectroscopy and cqed experiments," *New Journ. of Phys.*, vol. 3, pp. 14.1, 2001.

[38] F. Mugele and J. C. Baret, "Electrowetting: from basics to applications," *J. Phys.: Condens. Matter*, vol. 17, pp. 705-774, 2005.

[39] B. Shapiro, H. Moon, R. L. Garrell, and C. J. Kim, "Equilirium behavior of sesile drops under surface tension, applied external fields, and material variations," *J. Appl. Phys.*, vol. 93, pp. 5794-5811, 2003.

[40] V. H. Kwong, A. M. Mossman, and A. L. Whitehead, "Control of reflectance of liquid droplets by means of electrowetting," *Appl. Opt.*, vol. 43, pp. 808, 2004.

[41] R. J. Hopkins, R. Symes, R. M. Sayer, and J. P. Reid, "Determination of the size and composition of multicomponent ethanol/water droplets by cavity-enchanced Raman scattering," *Chem. Phys. Lett.*, pp. 665-672, 2003.

[42] L. Mitchem, J. Buajarern, R. J. Hopkins, A. D. Ward, R. J. J. Gilham, R. L. Johnston, and J. P. Reid, "A strategy for characterizing the mixing state of immiscible aerosol components and the formation of multiphase aerosol particles through coagulation," *J. Phys. Chem. A*, vol. 110, pp. 8116-8125, 2006.

[43] G. Gouesbet, B. Maheu, and G. Grehan, "Light scattering from a sphere arbitrarily located in a Gaussian beam, using a Bromwich formulation," *J. Opt. Soc. Am. A*, vol. 5, pp. 1427-1443, 1988.

[44] J. A. Lock, "Improved Gaussian beam-scattering algorithm," *Appl. Opt.*, vol. 34, pp. 559-570, 1995.

[45] S. L. McCall, A. F. J. Levi, R. E. Slusher, S. J. Pearton, and R. A. Logan, "Whispering-gallery mode microdisk lasers," *Appl. Phys. Lett.*, vol. 60, pp. 289, 1992.

[46] J. L. Jewell, S. L. McCall, Y. H. Lee, A. Scherer, A. C. Gossard, and J. H. English, "Lasing characteristics of GaAs microresonators," *Appl. Phys. Lett.*, vol. 54, pp. 1400, 1989.

[47] H.-M. Tzeng, K. F. Wall, M. B. Long, and R. K. Chang, "Laser emission from individual droplets at wavelengths corresponding to morphology-dependent resonances," *Opt. Lett.*, vol. 9, pp. 499-501, 1984.

[48] A. Kiraz, A. Sennaroglu, S. Doganay, M. A. Dündar, A. Kurt, H. Kalaycioglu, and A. L. Demirel, "Lasing from single, stationary, dye-doped glycerol/water microdroplets located on a superhydrophobic surface," *Opt. Commun.*, vol. 276, pp. 145-148, 2007.

[49] A. Einstein, "On the Quantum Theory of Radiation," *Physikalische Zeitschreibung*, vol. 18, pp. 121-128, 1917.

[50] P. W. Milonni and J. H. Eberly, *Lasers*. New York: John Wiley & Sons, 1988.

[51] A. E. Siegman, *Lasers*. California: University Science Books, 1986.

[52] O. Svelto, *Principles of Lasers*. New York: Plenum Press, 1998.

[53] J. B. Snow, S.-X. Qian, and R. K. Chang, "Stimulated Raman scattering from individual water and ethanol droplets at the morphology-dependent resonances," *Optics Letters*, vol. 10, 1985.

[54] S. Arnold and L. M. Folan, "Fluorescence spectrometer for a single electrodynamically levitated microparticle," *Rev. Sci. Instrum.*, vol. 57, pp. 2250-2253, 1986.

[55] R. J. Hopkins, L. Mitchem, A. D. Ward, and J. P. Reid, "Control and Characterisation of a single aerosol droplet in a single-beam gradient-force optical trap," *PCCP*, vol. 6, pp. 4924-4927, 2004.

[56] A. Sennaroglu, A. Kiraz, M. A. Dündar, A. Kurt, and A. L. Demirel, "Raman lasing near 630 nm from stationary glycerol-water microdroplets on a superhyrophobic surface," *to appear in Opt. Lett*, 2007.

[57] C. V. Raman, *Molecular Diffraction of Light*. Calcuta: Calcuta University Press, 1922.

[58] G. S. He and S. H. Liu, *Physics of Nonlinear Optics*. Singapore: World Scientific, 1999.

[59] N. Bloembergen and Y. R. Shen, "Coupling between vibrations + light waves in Raman laser media," *Phys. Rev. Lett.*, vol. 12, pp. 504, 1964.

[60] S. M. Spillane, T. J. Kippenberg, and K. J. Vahala, "Ultralow-threshold Raman laser using a spherical dielectric microcavity," *Nature*, vol. 415, pp. 621-623, 2002.

[61] H. C. T. E. M. Purcell and R. V. Pound, "Resonance Absorption by Nuclear Magnetic Moments in a Solid," *Phys. Rev.*, vol. 69, pp. 681, 1946.

[62] T. J. Kippenberg, "Fabrication, Coupling and Nonlinear Optics of Ultra High-Q Microcavities," in *Optical Microcavities*, K. Vahala, Ed. Singapore: World Scientific, 2004.

[63] R. J. Hopkins, L. Mitchem, A. D. Wardw, and J. P. Reid, "Control and characterisation of a single aerosol droplet in a single-beam gradient-force optical trap," *Phys. Chem. Chem. Phys.*, vol. 6, pp. 4924-4927, 2004.

[64] S. Arnold and L. M. Folan, "Fluorescence spectrometer for a single electrodynamically levitated microparticle," *Rev. Sci. Inst.*, vol. 57, pp. 2250-2253, 1986.